Intact Drosophila Central Nervous System Cellular Quantitation reveals Sexual Dimorphism

Wei Jiao[1], Gard Spreemann[1†], Evelyne Ruchti[1], Soumya Banerjee[1], Samuel Vernon[1], Ying Shi[1], R. Steven Stowers[2], Kathryn Hess[1] and Brian D. McCabe[1*].

1. Brain Mind Institute, EPFL - Swiss Federal Institute of Technology Lausanne, Switzerland.
2. Department of Microbiology and Cell Biology, Montana State University, Bozeman, U.S.A

[†] Current address: Telenor Research, Fornebu, Norway

*To whom correspondence should be addressed: brian.mccabe@epfl.ch

ABSTRACT

Establishing with precision the quantity and identity of the cell types of the brain is a prerequisite for a detailed compendium of gene and protein expression in the central nervous system. Currently however, strict quantitation of cell numbers has been achieved only for the nervous system of *C.elegans*. Here we describe the development of a synergistic pipeline of molecular genetic, imaging, and computational technologies designed to allow high-throughput, precise quantitation with cellular resolution of reporters of gene expression in intact whole tissues with complex cellular constitutions such as the brain. We have deployed the approach to determine with exactitude the number of functional neurons and glia in the entire intact larval *Drosophila* central nervous system (CNS), revealing fewer neurons and more glial cells than previously predicted. We also discover an unexpected divergence between the sexes at this juvenile developmental stage, with the female CNS having significantly more neurons than that of males. Topological analysis of our data establishes that this sexual dimorphism extends to deeper features of CNS organisation. We additionally extended our analysis to quantitate the expression of voltage-gated potassium channel family genes throughout the CNS and uncover substantial differences in abundance. Our methodology enables robust and accurate quantification of the number and positioning of cells within intact organs, facilitating sophisticated analysis of cellular identity, diversity, and gene expression characteristics.

INTRODUCTION

Establishing the precise number of cells in the brain is essential to create organ-wide catalogues of cell-types and their gene expression (Lent et al., 2012; Devor et al., 2013). However, apart from the nervous system of the nematode *Caenorhabditis elegans* [302 neurons, 56 glia] (White et al., 1986), the exact numbers of cells within the central nervous system (CNS) of model organisms or that of humans is currently unknown, with estimates, including those based upon extrapolation from direct quantification of brain sub-regions, varying widely (Silbereis et al., 2016; Keller et al., 2018; von Bartheld et al., 2016).

Studies of the CNS of *Drosophila melanogaster*, which in scale and behavioural repertoire has been viewed as intermediate between nematodes and rodents (Bellen et al., 2010; Alivisatos et al., 2012), currently include large-scale efforts to establish both a neuronal connectome and cell atlas (Scheffer and Meinertzhagen, 2019; Allen et al., 2020; Li et al., 2022). Nonetheless, the precise numbers of cells (neurons or glia) in either the smaller larval or larger adult *Drosophila* CNS, comprised of both a brain and Ventral Nerve Cord (VNC), remain unknown, though several approximations have been suggested. For the larval CNS, a range of between 10,000 to 15,000 active neurons has been proposed (Scott et al., 2001; Meinertzhagen, 2018; Eschbach and Zlatic, 2020) across developmental timepoints. For adult Drosophila, approximations have been suggested in the range of between 100,000 to 199,000 neurons in the brain (Simpson, 2009; Chiang et al., 2011; Kaiser, 2015; Scheffer and Meinertzhagen, 2019; Raji and Potter, 2021) together with between 10,000 to 20,000 cells in the VNC (Birkholz et al., 2015; Lacin et al., 2019; Bates et al., 2019; Allen et al., 2020). The other major CNS cell type, glia, has been estimated to be approximately 10% of the number of neurons (Kremer et al., 2017; Meinertzhagen, 2018; Raji and Potter, 2021). Given the large diversity of these estimates, precise quantification of the numbers of *Drosophila* neurons and glia would seem a desirable goal, beginning with the smaller larval CNS which enables the wide compendium of larval *Drosophila* behaviours (Gerber et al., 2009; Neckameyer and Bhatt, 2016; Eschbach and Zlatic, 2020; Louis, 2020; Gowda et al., 2021).

Complicating the aspiration quantitate the *Drosophila* larval CNS, in addition to the general problem of separating and quantifying primary cell types such as neurons and glia, are two specific confounding factors that limit simple total cell quantification approaches. Firstly, encompassed within and surrounding the larval CNS are dividing neuroblasts, which will give rise to adult neurons (Doe, 2017). Relatedly, imbedded within the larval CNS are substantial numbers of immature adult neurons, observed from electron micrograph reconstructions as having few or no dendrites and axons that terminate in filopodia lacking synapses (Eichler et al., 2017). These immature neurons are unlikely to contribute to larval CNS function and are generally excluded when considering larval neuronal circuit architecture (Eichler et al., 2017; Scheffer and Meinertzhagen, 2019). It has been suggested that only a small fraction of the total number of larval CNS cells may actually contribute to CNS function (Ravenscroft et al., 2020).

Here we have sought to develop a synergistic molecular genetic, imaging, and computational pipeline designed *de novo* to allow automated neuron, glia, or other gene expression features to be precisely quantitated with cellular resolution in intact whole central nervous systems. Central to the approach are high signal-to-noise gene expression reporters that produce a punctate, nucleus-localised output facilitating downstream automated computational measurement and analysis. Exploiting multiple genetic reagents designed to selectively identify only functional neurons with active synaptic protein expression, we identify substantially fewer neurons than most previous estimates in the *Drosophila* larval CNS, and in addition, substantially more glia. We also discover a previously unsuspected sexual dimorphism in the numbers of both cell types at larval stages. The generation of whole CNS point clouds from our data enabled us to apply the tools of topological data analysis to summarize the CNS in terms of multi-scale topological structures. Utilization of these topological summaries in a support vector machine also supports that sexual dimorphism extends to deeper features of CNS organisation. Finally, we applied our pipeline to quantitate the whole CNS expression frequency of the *Drosophila* family of voltage-gated potassium channels which revealed divergent channel expression frequency throughout the CNS. We envision that our method can be employed to allow precise quantitation of gene expression characteristics of the constituent cells of

57 the brain and potentially other intact whole organs in a format suitable for sophisticated downstream
58 analysis.
59
60 **RESULTS**
61 **Genetic and imaging tools designed to facilitate automated whole CNS cellular quantitation.**
62 To establish a robust quantitative method to measure gene expression frequency and quantify the
63 cell numbers that contribute to *Drosophila* larval CNS function, we sought to develop a pipeline
64 utilising genetic reporters designed to expediate automated neuron and glia quantitation from three-
65 dimensional intact organ images. While membrane associated reporters are generally employed to
66 label *Drosophila* neurons (Pfeiffer et al., 2008; Jenett et al., 2012; Ravenscroft et al., 2020), we
67 generated UAS-driven (Brand and Perrimon, 1993; Wang et al., 2012) fluorescent reporters fused
68 to Histone proteins (Sherer et al., 2020) to target fluorescence only to the nucleus, in order to
69 facilitate subsequent automated segmentation and counting. Through empirical selection of
70 transgene genomic integration sites, we established a set of reporter lines that produced a strong
71 and specific punctate nucleus signal when expression is induced, with little to no unwanted
72 background expression. We then developed a procedure to capture the entire micro-dissected larval
73 CNS volume by light sheet microscopy at multiple angles and with high resolution, imaging only
74 animals within the ~two-hour developmental time window of the wandering third instar larval stage
75 (Ainsley et al., 2008). These multi-view datasets were then processed to register, fuse, and
76 deconvolve the entire larval CNS volume. The volume was then segmented and cell numbers
77 automatically quantified (Figure 1a-d).
78
79 To evaluate the reliability of the procedure, we began by comparing automated counts of distinct
80 neuronal subtypes with manual counting. We separately labelled all dopaminergic neurons (Figure
81 1e) [TH-GAL4](Friggi-Grelin et al., 2003a; Mao and Davis, 2009), serotonergic neurons (Figure
82 1f)[Trh-GAL4] (Alekseyenko et al., 2010), and neurons that produce both types of neurotransmitter
83 (Figure 1g)[Ddc-GAL4] (Lundell and Hirsh, 1994) in the larval CNS. Quantification revealed a high
84 level of concordance (Figure 1h, +/-0.21%, n= 5 for TH-GAL4, +/-1%, n= 5 for Trh-GAL4, +/-0.38%,

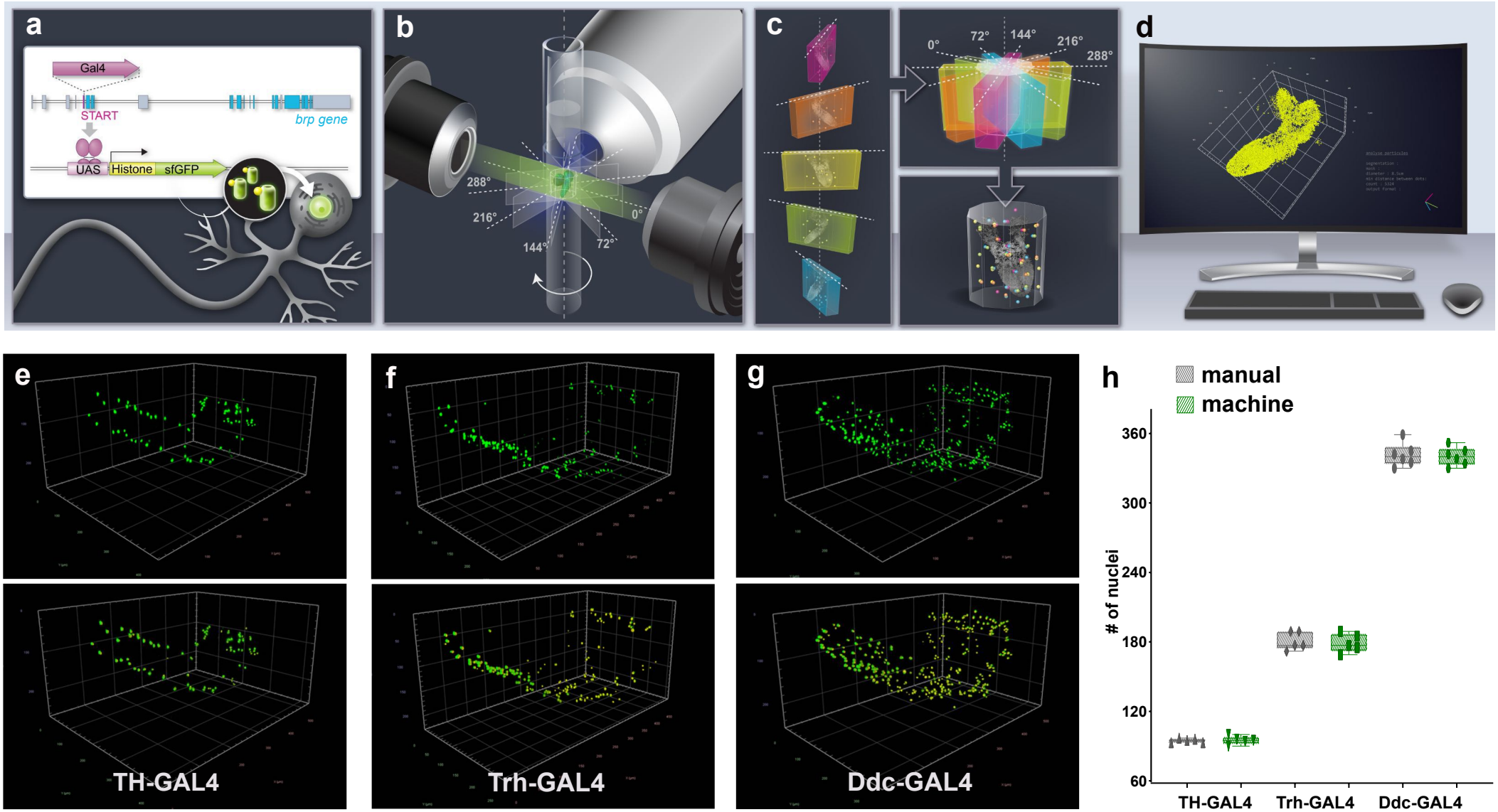

Figure 1. Intact whole CNS quantitation pipeline schematic and validation.
(**a-d**) Illustration of intact whole CNS genetic, imaging and computational pipeline. (**a**) Genetic reagents: GAL4 is introduced to the exonic sequences of genes encoding synaptic proteins (e.g. *brp*) to capture their expression pattern with high fidelity. GAL4 expression regulates the production of UAS fluorescent-histone reporters which target to the nucleus of cells producing a punctate signal. (**b**) Imaging: The intact CNS is imaged at high resolution using light-sheet microscopy. Images are captured at 5 different angles with 72-degree intervals. (**c**) Assembly: multiview light sheet images are registered, fused and deconvolved. (**d**)Quantitation: volume is segmented, nucleus number and relative position is measured. Three dimensional co-ordinates of the geometric center of every nucleus can be calculated to produce a point cloud of nuclei positions.(**e-h**) Pipeline validation. Three dimensional images before (above) and after (below) segmentation panels of (**e**) dopaminergic [TH-GAL4] neurons, (**f**) serotonergic neurons [Trh-GAL4] and (**g**) dopa decarboxylase expressing [Ddc-GAL4] neurons. (**h**) Manual or automated quantification of nuclei numbers in these volumes are similar. Scale squares in **e** and **g** is 100μm and in **f** is 50μm.

85 n= 6 for Ddc-GAL4, Figure 1-source data 1) between automated and manual measurements of these
86 neuronal subtypes establishing confidence in the procedure.
87
88 **Number of neurons and glia in the female larval CNS.** Encouraged by our neuronal subset
89 quantitation results, we next sought to generate GAL4 lines for genes likely to be expressed only in
90 active larval neurons with synaptic connections but not by neuroblasts or by immature neurons
91 (Figure 2-figure supplement 1). We biased towards generating GAL4 insertions within endogenous
92 genomic loci in order to reproduce endogenous patterns of gene expression with high fidelity.
93
94 Bruchpilot (Brp) is a critical presynaptic active zone component widely used to label *Drosophila*
95 synapses, including for large-scale circuit analyses (Wagh et al., 2006). We employed CRISPR/Cas9
96 genome editing to insert GAL4 within exon 2 of the *brp* gene, utilising a T2A self-cleaving peptide
97 sequence (Diao et al., 2015) to efficiently release GAL4. While this exonic insertion generated a
98 hypomorphic allele of *brp* (data not shown) when homozygous, the line was employed in
99 heterozygotes to capture Brp protein expression with high fidelity. To complement this line, we used
100 the Trojan/MiMIC technique (Diao et al., 2015), to generate a GAL4 insertion in the *syt1* gene, which
101 encodes Synaptotagmin 1 (Littleton et al., 1994), the fast calcium sensor for synaptic
102 neurotransmitter release (Quiñones-Frías and Littleton, 2021). Lastly, we examined a transgenic line
103 where the promoter of *nsyb* (*neuronal synaptobrevin*) (Deitcher et al., 1998), which encodes an
104 essential presynaptic vSNARE (Südhof and Rothman, 2009), is used to control GAL4 expression
105 (Aso et al., 2014). All three lines were expressed in a similar pattern, labelling a substantial fraction
106 but not all of the total cells in the larval CNS (Figure 2a-c). These lines contrasted with the widely
107 used elav-GAL4 (Lin and Goodman, 1994), which was expressed in larval neurons, but also
108 apparently in some immature neurons and potentially in some glia as well (Berger et al., 2007)
109 (Figure 1-figure supplement 1). To characterise our lines, we examined their expression throughout
110 development beginning with embryogenesis. We detected no expression from any of the three lines
111 prior to embryonic stage 16 (Figure 2-figure supplement 2a). However, beginning at stage 17 of
112 embryonic development, when synaptic activity begins (Baines and Bate, 1998), all three lines

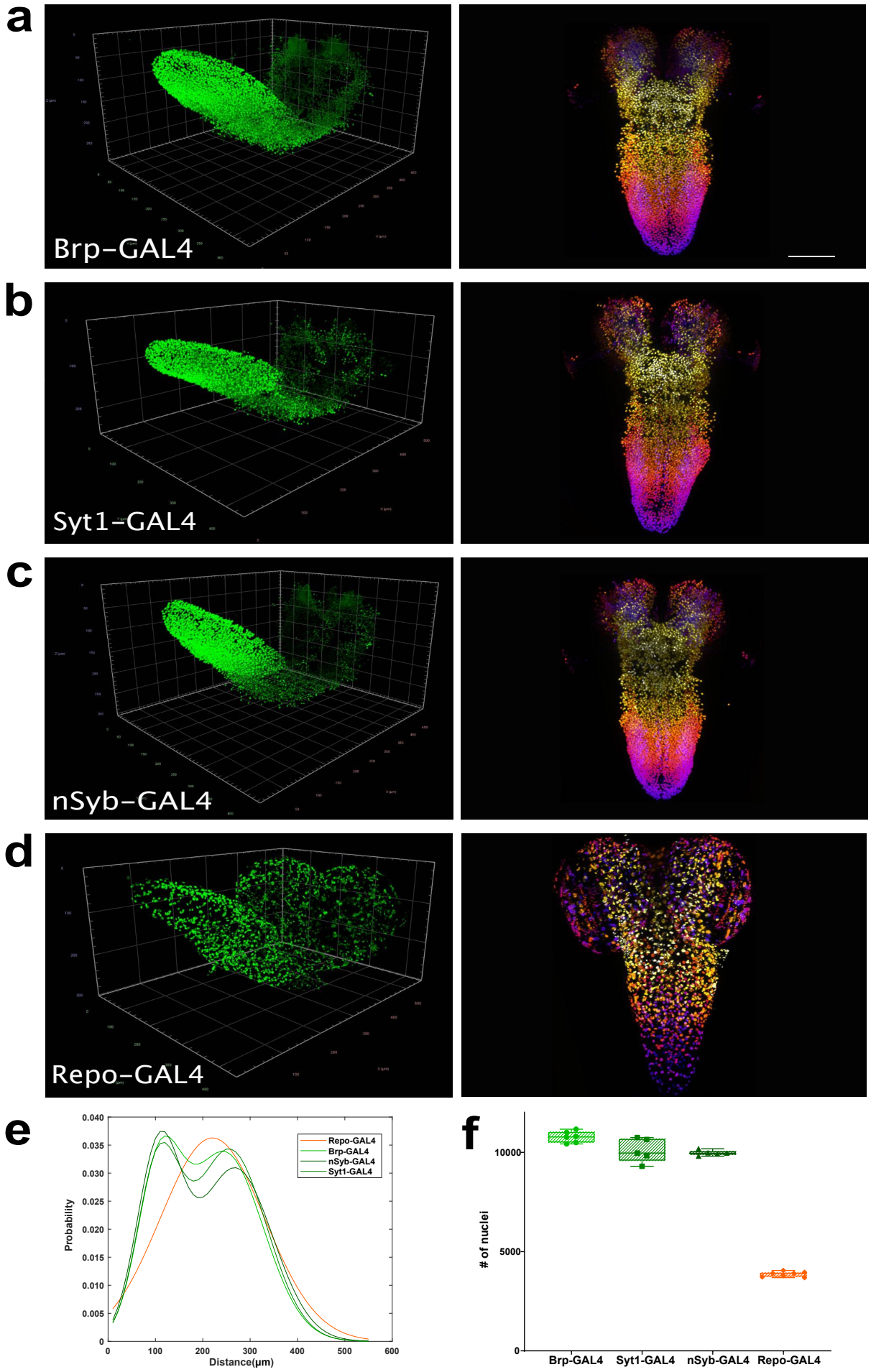

Figure 2. Whole CNS quantitation of neurons and glia in the female larval brain.
(**a-d)** Multiview deconvolved images (left) and z-stack projections (right) [colours represent z position] of the CNS of (**a**) Brp-GAL4, (**b**) Syt1-GAL4, (**c**) nSyb-GAL4 and (**d**) Repo-GAL4. (**e**) Distribution of inter-nuclei distances for each line. (**f**) Quantification of the number of labelled nuclei in each line. **a-d**: left; scale squares **a** and **c** = 50μm, **b** and **d** = 100μm; right images identical magnification, scale bar = 100μm.

Jiao et al. Figure 2

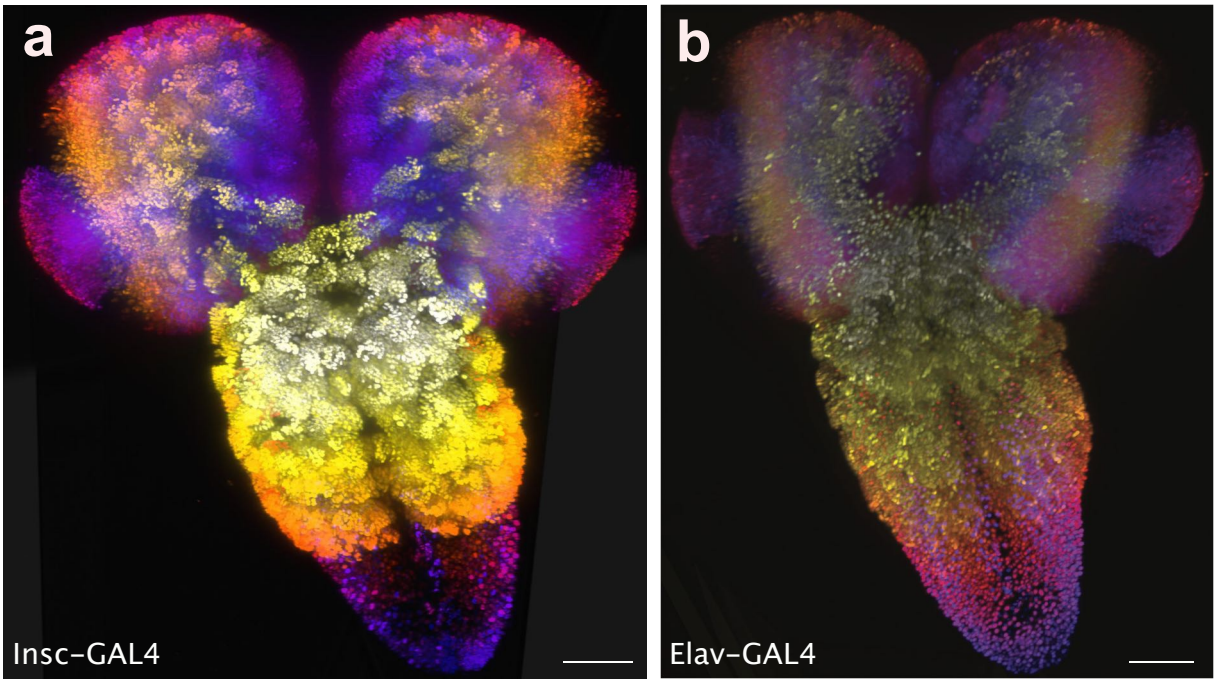

Figure 2-figure supplement 1. CNS projections labelled with **(a)** Insc-GAL4 and **(b)** Elav-GAL4. Insc-GAL4 labels neuronal stem cells. Elav-GAL4 also labels a fraction of stem cells in addition to potentially glial cells. Colours represent z position. Scale bar: 50μm

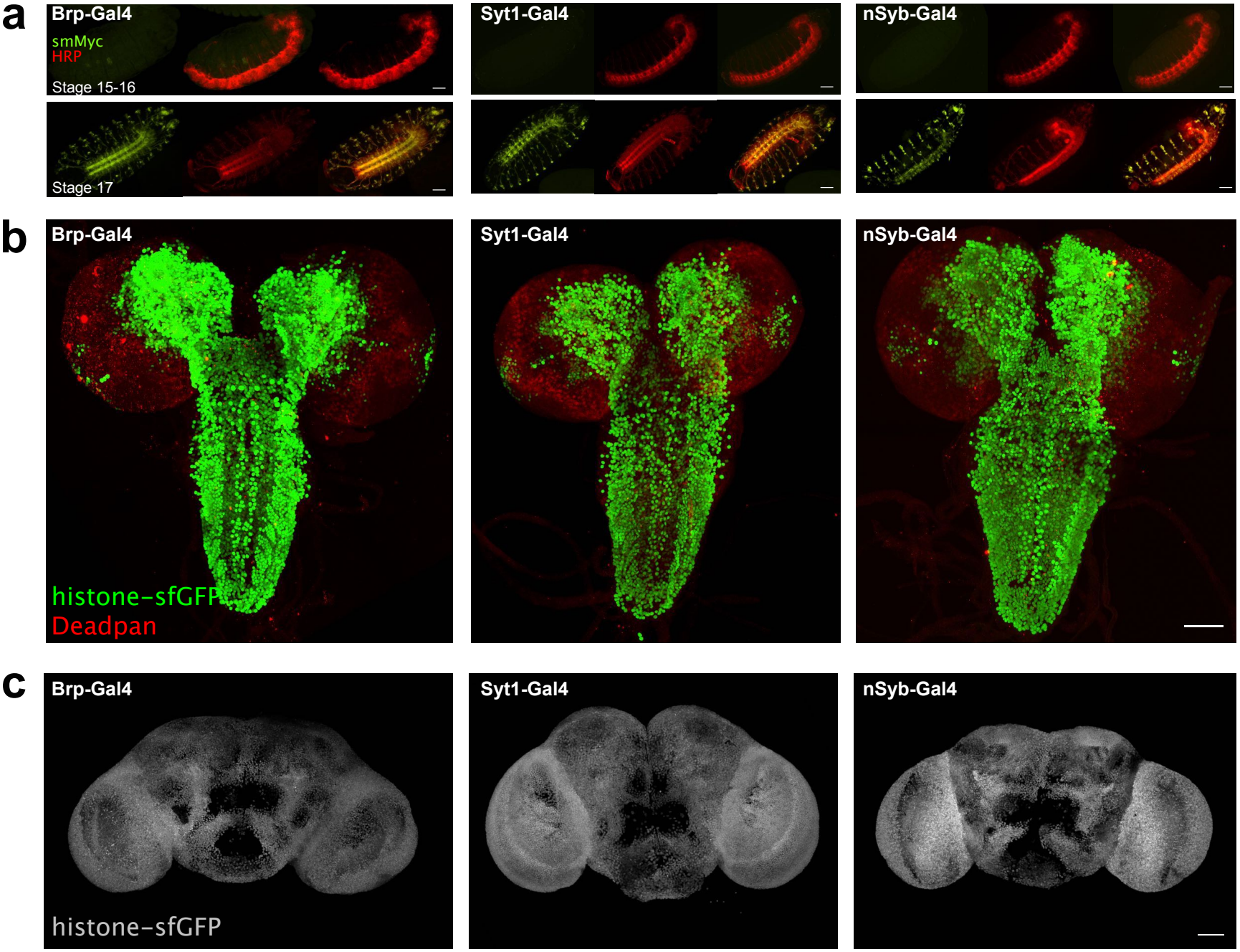

Figure 2-figure supplement 2. (a) Expression UAS>smFP[myc] (green) under control of Brp-Gal4, Syt1-Gal4 and nSyb-Gal4 in embryonic stages 15-16 (upper) and stage 17 (lower). Neuronal membranes are labelled with HRP (red) **(b)** Labeling of L3 larval CNS with Deadpan (red) and UAS>histone-sfGFP (green) under control of Brp-Gal4, Syt1-Gal4 or nSyb-Gal4**(c)** histone-sfGFP expression in the adult brain under control of Brp-Gal4, Syt1-Gal4 and nSyb-Gal4.

scale bar = 50μm in **(a)**, **(b)** and **(c)**

113 displayed expression in both the peripheral and central nervous system (Figure 2-figure supplement
114 2). We also examined if these lines were expressed in neural stem cells during larval stages by co-
115 labelling the larval CNS with the transcription factor Deadpan, a neuroblast marker (Bier et al., 1992).
116 We found that labelling by all three lines did not overlap with Deadpan expression (Figure 2-figure
117 supplement 2), suggesting these lines are not expressed in neuroblasts. We also examined
118 expression all three lines in the adult brain and, as in the larval CNS, observed labelling of a large
119 fraction but not all of the total cells in the adult brain (Figure 2-figure supplement 2). Lastly, to ensure
120 that the cells labelled by our lines were exclusively neurons, we compared their expression to that
121 of glial cells labelled by glial specific transcription factor Repo (Xiong et al., 1994; Lin and Potter,
122 2016) using independent and mutually exclusive QF2 dependent labelling. We found complete
123 exclusion of cells labelled by Brp, Syt and nsyb from cells labelled by Repo (Figure 2d), consistent
124 with the Brp, Syt1 and nsyb Gal4 lines labelling only neurons that express synaptic protein genes
125 but not glial cells.
126
127 To further compare these lines, beginning with the CNS of female animals, we calculated three
128 dimensional coordinates for the geometric center of all nuclei labelled in the Brp, Syt1 and nSyb
129 GAL4 lines to generate point cloud mathematical objects and compared them to point clouds of glial
130 nuclei labelled by the Repo GAL4 line. We then plotted and compared the distributions of inter-
131 nuclei distances in these lines. Using this measurement, we found that inter-nuclei distance of glial
132 cell nuclei exhibited a unimodal distribution (Figure 2e). In contrast, all three neuronal lines exhibited
133 a bimodal distribution of inter-nuclei distances (Figure 2e). We thus observed two patterns of labelled
134 nuclei, one shared among neuronal lines and the other distinct for glia (Figure 2e), again consistent
135 with these lines labelling different cell types.
136
137 We next counted the number of nuclei labelled by these neuronal and glial lines, again beginning
138 with females (Figure 2f). We found that the CNS labelled by Brp-Gal4 had 10776(+/- 2.65%, n= 6)
139 neurons, Syt1-Gal4 had 10097(+/- 5.96%, n= 5) neurons and nSyb-Gal4 had 9971(+/- 1.35%, n= 5)
140 neurons (Figure 2f). We tested the statistical difference in the numbers of neurons labelled by these

141 lines and found that while nSyb-GAL4 and Syt1-GAL4 were not statistically different from each other,
142 Brp-GAL4 did label significantly more neurons than either Syt1 or nSyb (Brp-GAL4 vs Syt1-GAL4 +
143 6.72%, p=0.03, Brp-GAL4 vs nSyb-GAL4 + 8.07% p=0.01). Averaging across the lines, we found
144 that the female third instar larval CNS had 10312 +/- 5.03%, n=16 neurons (Figure 2-source data 1).
145 To ensure that our method did not introduce bias in dense data sets, we also manually counted a
146 Brp-GAL4 labelled CNS and compared it to the automated count. Similar to our experiments with
147 sparse neuronal labelling, we found good agreement between manual and automated quantification
148 with a difference of just 14 neurons (9430 nuclei manual vs 9444 nuclei automated for this individual
149 CNS).
150
151 We next counted the number of glia labelled by the Repo GAL4 line (Figure 2d,f). We measured
152 3860 +/- 3.37%, n=7 glia in the female CNS (Figure 2-source data 1). This amounted to 37% of the
153 number of neurons, far more than the previously estimated (Meinertzhagen, 2018; Raji and Potter,
154 2021). In sum, we found that the female *Drosophila* larval CNS had 10312 neurons, fewer than most
155 previous predictions and several fold more glia that previously thought.
156
157 **Males have fewer neurons and more glia than females.** We next carried out a similar analysis on
158 the CNS of male larvae (Figure 3a-c). We found that Brp-GAL4 labelled 9888 (+/-3.15%, n= 5)
159 neurons, Syt1-GAL4 labelled 9012 (+/-3.8%, n= 5) neurons, and nSyb-GAL4 labelled 9286 (+/-
160 5.38%, n= 5) neurons in male larvae (Figure 3e, Figure 3-source data 1). In males, Brp-GAL4 did
161 not label significantly more neurons than nSyb-GAL4 but did label more than Syt1-GAL4 (Brp-GAL4
162 vs Syt1-GAL4 + 876, p=0.01), while the number of neurons labelled by nSyb-GAL4 was not
163 significantly different from Syt1-GAL4, as we had found in females. Averaging across the lines we
164 found that the male third instar larval CNS had 9396 +/- 5.59%, n= 15 neurons, significantly fewer
165 than those of females (-9.75%, P<0.0001). This difference was also consistent within individual
166 genotypes with Brp-GAL4 labelling (-8.98%, P=0.0008), Syt1-GAL4 labelling (-12.04%, P=0.008)
167 and nSyb-GAL4 labelling (-7.38%, P=0.0182) less neurons in males than in females.
168

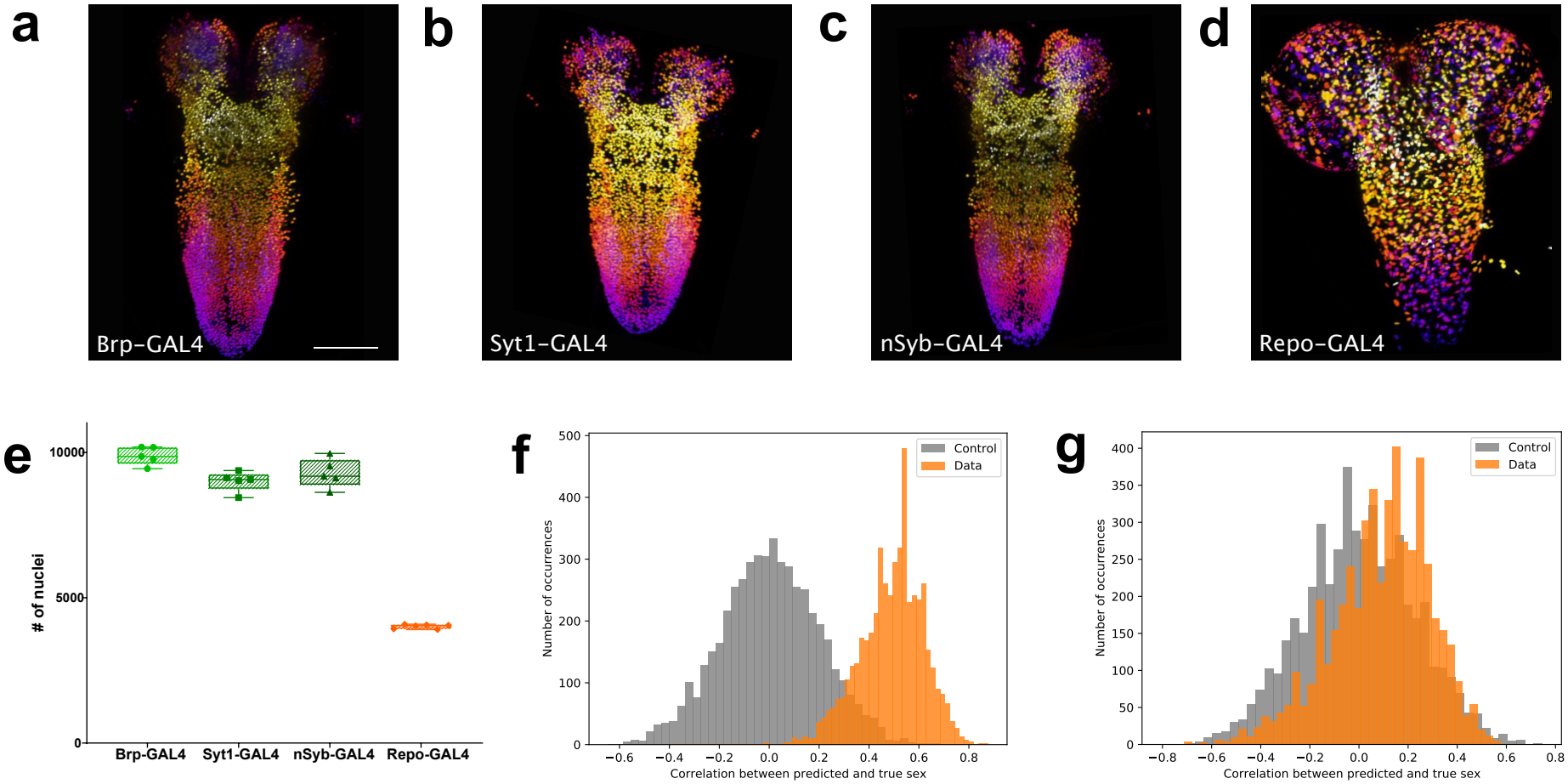

Figure 3. Quantitation of neurons and glia in the male larval CNS and topological comparison of sex differences. (**a-d**) Example z-stack projections [colours represent z position] of male larval CNS of (**a**) Brp-GAL4, (**b**) Syt1-GAL4, (**c**) nSyb-GAL4 and (**d**) Repo-GAL4.(**e**) Quantification of the number of labelled nuclei in each line. (**f**) The distribution of correlations between the ground truth and the prediction made by the SVM using topological features is indicative of sexual dimorphism of the higher order structure of neuron point clouds (**g**) Simpler point cloud features such as properties of the distributions of inter-nuclei distances are not indicative of this. **a-d**: identical magnification, scale bar =100μm

Jiao et al. Figure 3

We also counted the number of glia labelled by Repo-GAL4 in males (Figure 3d, e). We found that males had 4015 glia, again far more than previous estimates (Figure 3-source data 1). The number of glia in the male larval CNS was also significantly more than in females (+3.86%, P=0.0284). In summary, male *Drosophila* larva have significantly fewer CNS neurons than females but significantly more glia.

Topological analysis detects significant structural differences between males and females. We next wished to determine whether the differences between the point clouds derived from the positions of neuronal nuclei of males and females went beyond simple numerics. To do this we applied the tools of topological data analysis (Rabadan and Blumberg, 2019; Chazal and Michel, 2021) to summarize the CNS in terms of multi-scale topological structures (Expert et al., 2019). These topological summaries, the construction of which is described in the methods, can be thought of as multi-scale descriptions of the shape of the data set. Topological summaries, which can be compared by standard methods despite the lack of common reference points, could then be used as the classification features in a support vector machine (SVM). Since the total number of point clouds was relatively small for this type of analysis, we down-sampled each whole CNS point cloud randomly to 8000 points 100 times, producing a total of 3100 point clouds, for each of which we then computed a certain topological summary, called the *degree-1 persistence diagram of its alpha complex* (Edelsbrunner and Mücke, 1994).

After fixing the necessary hyperparameters, sex classification experiments were run across 5000 random train/test splits of the topological summaries. In each split, the summaries derived from subsamplings of a single point cloud (CNS) were either all in the training set or all in the testing set, to avoid leaking information. Each time, the SVM was trained once with the animal's true sex as the target class and once with a randomly assigned sex as the target, as a control. We then computed the Pearson correlation between the classifier's output on the testing set and the true (respectively randomized) sex of the animal.

197 The 5000 splits were used to produce 5000 correlations with the true sex and 5000 correlations with
198 a randomly assigned sex. The distribution of these correlations (Figure 3f), exhibiting clearly that the
199 SVM is able to extract the sex of the animal reliably: only about 1.9% of the splits result in a higher
200 correlation in the control set than in the true data. Moreover, repeating the procedure with simpler
201 point cloud features, like properties of the distributions of inter-nuclei distances, did not produce a
202 significant signal (Figure 3g). Thus, the pattern, which seems hard to describe concisely, is not
203 revealed through simpler descriptors of the neuron configurations, leading us to suspect CNS sexual
204 dimorphism extends to deeper features of organisation that are both subtle and widely distributed.
205 These results, in addition to the differences in total cell numbers, support sexual dimorphism of the
206 male and female CNS at the larval stage.
207
208 **Potassium channel family members have different densities in the CNS**. Having established a
209 baseline of total numbers of neurons in the larval CNS, we next sought to deploy the quantification
210 pipeline to measure the expression frequency of key neuronal function genes throughout the CNS.
211 We chose to examine the family of voltage-gated potassium channels, which are essential for many
212 aspects of neuronal function and for which *Drosophila* studies defined the founding members
213 (McCormack, 2003). We generated GAL4 insertions in the Shaker (Sh) [Kv1 family], Shab (Sb) [Kv
214 2 family], Shaw (Sw) [Kv3 family] and Shal (Sl) [Kv4 family](McCormack, 2003) genes using the
215 Trojan/Mimic technique (Diao et al., 2015). As the Sh gene is x-linked, we carried out our
216 quantitation analysis in the male CNS only to avoid potential gene dosage effects. To determine
217 whether our GAL4 reporter lines had patterns of expression consistent with the known properties of
218 these channels, we examined the expression of all four lines in motor neurons, where functional
219 activity for Shaker, Shab, Shaw and Shal has previously been demonstrated by electrophysiological
220 measurements (Covarrubias et al., 1991; Ryglewski and Duch, 2009). We found that the GAL4
221 reporters for all 4 channels were expressed as expected in motor neurons (Figure 4-figure
222 supplement 1), consistent with accurate reproduction of the established expression of these proteins.
223

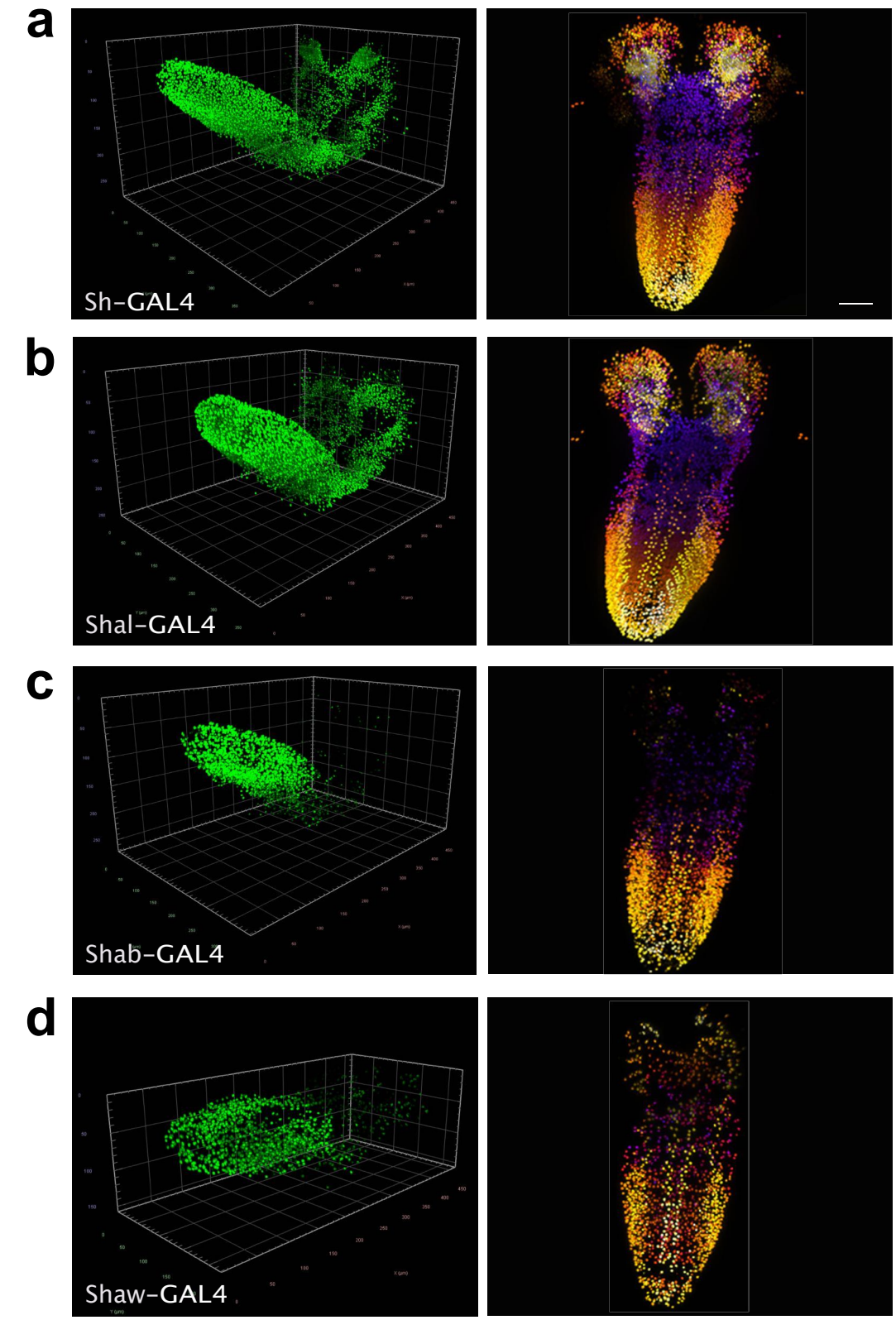

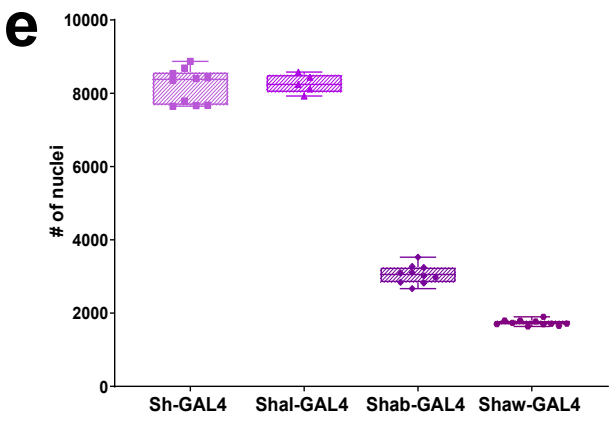

Figure 4. Quantitation of the number of neurons expressing voltage-gated potassium channels. (**a-d**) Multiview deconvolved images (left) and z-stack projections (right) [colours represent z position] of potassium channel family members: (**a**) Sh-GAL4, (**b**) Shal-GAL4, (**c**) Shab-GAL4 and (**d**) Shaw-GAL4. (**e**) Quantification of the number of labelled nuclei in each line. **a-d**: left, scale squares = 50µm, right, identical magnification, scale bar = 50µm.

Jiao et al. Figure 4

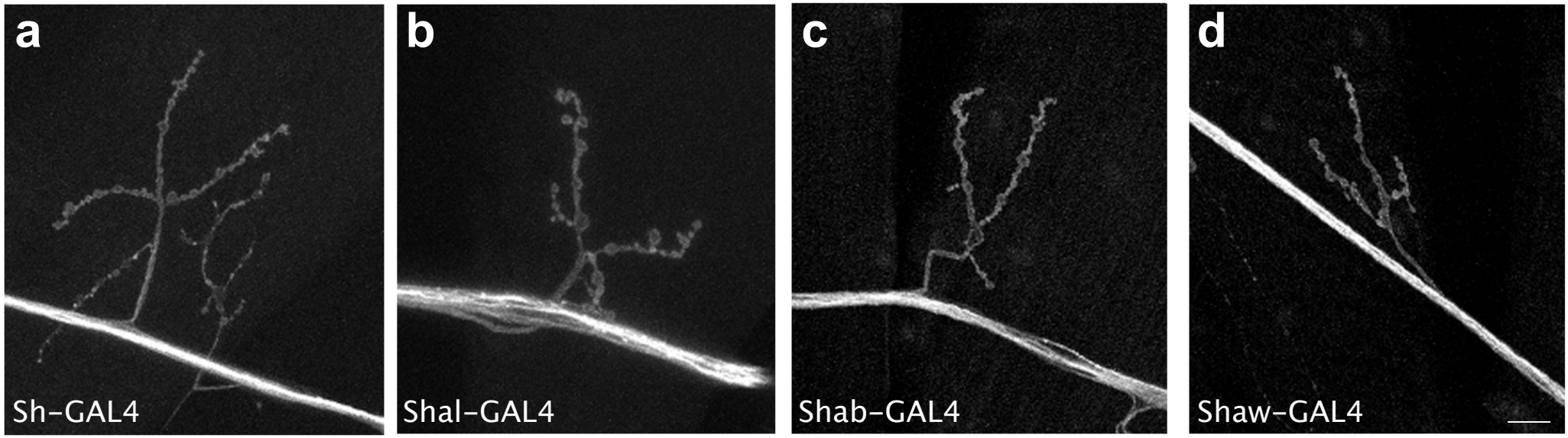

Figure 4-figure supplement 1. Expression in example motor neurons and neuromuscular junction terminals of UAS>mKO-CAAX by **(a)** Sh-GAL4, **(b)** Shal-GAL4, **(c)** Shab-GAL4 and **(d)** Shaw-GAL4. All four lines express in motor neurons as predicted from mutant analysis. All images identical magnification, scale bar = 10μm.

Jiao et al. Figure 4-figure supplement 1

224 We next examined the expression frequency of these genes in the entire CNS (Figure 4a-d). We
225 found that Shaker and Shal were expressed in large numbers of neurons 8204 +/- 5.67% and 8261
226 +/- 3.1%, though significantly less (-12.7 % and -12.1% $p<0.0001$) than the average number of all
227 male neurons (Figure 4 a,b,e, Figure 4-source data 1). In contrast, Shab (3057+/- 8.21% n=10) and
228 Shaw (1737 +/- 4.3% n=11) were expressed in smaller numbers of neurons (Figure 4c-e), with
229 expression observed in only 32.5% or 18.5% of total male neurons respectively, suggesting more
230 discrete functions within CNS neurons and contrasting with the collective expression of all four genes
231 within motor neurons (Figure 4-figure supplement 1). In particular, Shab and Shaw had very reduced
232 expression in the brain lobes of larva (Figure 4c,d) compared with Shaker and Shal (Figure 4a,b).
233 These results establish that our genetic-imaging pipeline can enable quantitation of the expression
234 frequency of families of genes essential for neuronal properties across the entire CNS.
235

236 **DISCUSSION**

237 Establishing the number and identity of cells in the CNS is a foundational metric upon which to
238 construct molecular, developmental, connectomic and evolutionary atlases of central nervous
239 systems across species (Lent et al., 2012; Devor et al., 2013). Here, we develop and deploy a
240 methodological pipeline to label discrete cell types in the intact *Drosophila* CNS, with genetic
241 reporters designed to facilitate the subsequent segmentation and automated quantification of cell
242 types, in addition to capturing positional coordinates of relative nucleus position throughout the
243 organ. Using this toolset, we find fewer active neurons, as defined by expression of synaptic protein
244 genes, in the *Drosophila* larval CNS than the majority of previous predictions and substantially more
245 glia. We also discover previously unsuspected differences in both neuron and glial density and CNS
246 topology at the larval stage, when external sex organs are absent, with females possessing both
247 more neurons and but fewer glia than males. Topological analysis of the point cloud derived from
248 neuronal nucleus position, which detects potentially subtle and complex geometric structure in the
249 data, also strongly supports the existence differences between males and females. In addition,
250 deploying these tools, we find that while all members of the *Drosophila* voltage-gated potassium
251 channel family are expressed in motor neurons, consistent with prior mutant analyses, the Kv2

252 channel Shab and Kv3 channel Shaw are expressed in a much smaller number of neurons in the
253 CNS than the Kv1 channel Shaker and the Kv4 channel Shal, suggesting conclusions drawn about
254 the coordinated activity of these channels from studies of motor neurons may not be broadly
255 applicable across the CNS, where the genes encoding these channels are frequently not co-
256 expressed.
257
258 A number of semi-quantitative methods have been employed to estimate the number of neurons in
259 the brains of humans and model organisms, including *Drosophila* (Lent et al., 2012; Keller et al.,
260 2018). For example, the number of neurons or other cells in the brain has been estimated using
261 stereological counting of sub-regions. A major limitation of this approach is the assumption of
262 homogenous cell density across the organ or within subregions, which is not supported by the high
263 variability of counts even between samples of similar regions, and thus likely introduces large errors
264 (von Bartheld et al., 2016; Keller et al., 2018). Rough extrapolation of neuronal counts of electron
265 microscope volumes of the regions of the *Drosophila* larval CNS had suggested an estimate of
266 ~15,000 neurons (Meinertzhagen, 2018; Eschbach and Zlatic, 2020). An alternate approach is
267 isotropic fractionation, where all cells in large regions or the entire CNS are dissociated to produce
268 a homogeneous single-cell suspension. Nuclei in the suspension can then be labelled by
269 immunohistochemistry and cells in a subvolume counted in a Neubauer chamber to estimate the
270 total number of cells present. Limitations of the approach include the necessity to ensure complete
271 dissociation of cells while avoiding tissue loss, the requirement for homogenous antibody labelling,
272 and highly accurate dilution (Deniz et al., 2018). This approach has recently been used to estimate
273 the total number of neurons and glia in the adult *Drosophila* brain and suggested a number of
274 199,000 neurons (Raji and Potter, 2021), twice prior estimates (Scheffer and Meinertzhagen, 2019;
275 Allen et al., 2020). In contrast to our results in the larval CNS, this study found no significant
276 differences in the number of neurons between the sexes and also found that 'non-neuronal' cells,
277 which should include glia, accounted for less than 9% of the total cells counted. In addition to the
278 inherent inaccuracy of the isotropic fractionation technique, which the authors both observed and
279 acknowledge (Raji and Potter, 2021), their use of anti-Elav antibody labelling, which can label some

280 glia in addition to neurons (Berger et al., 2007), or perhaps differences in life stage, may explain
281 some of the discrepancies between our results.
282
283 An unpredicted result from our whole CNS neuron quantitation was substantial differences in neuron
284 and glial numbers between the sexes in larva. In adult *Drosophila*, sexually dimorphic neural circuitry
285 has been observed in olfactory system (Kimura et al., 2005), and human females have also been
286 reported to have more olfactory bulb neurons and glia than males (Oliveira-Pinto et al., 2014). While
287 sex-specific behavioural differences are obvious in adult *Drosophila* (Jazin and Cahill, 2010), few
288 sexually dimorphic behavioural differences have been reported in larva (Aleman-Meza et al., 2015).
289 However male and female larva do differ in nutritional preference (Rodrigues et al., 2015; Davies et
290 al., 2018), which could potentially account for some aspects of the dimorphism we observe. In
291 addition to differences in total cell numbers, our topological methods, which take into account multi-
292 scale structure, suggests that differences in CNS structure between the sexes is both subtle (in the
293 mathematical sense) and non-localised in nature, and indeed are not observable with simpler
294 analysis methods of CNS organisation.
295
296 In addition to enabling precise counting of genetically labelled cells, our method allows the relative
297 measurement of discrete cell types or gene expression frequencies throughout the CNS. For
298 example, the relative frequency of glial cells to neurons in the human brain has been long been
299 debated (von Bartheld et al., 2016) and in the adult *Drosophila* brain it has been suggested there
300 are 0.1 glial per neuron (Kremer et al., 2017; Scheffer and Meinertzhagen, 2019; Raji and Potter,
301 2021). In the larval *Drosophila* CNS, we found closer to 0.4 glial cells per neuron on average, more
302 similar to the glial-neuron ratios reported for rodents or rabbits (Verkhratsky and Butt, 2018). An
303 important potential caveat however is that the large relative ratio of glia we observe in the third instar
304 larva could conceivably be glia produced in advance of adult CNS development. As adult specific
305 neuron numbers expand during pupation, the relative ratio of glia could potentially decline. Additional
306 glial-neuron ratio measurements in the adult CNS will be required to examine this possibility.
307

308 Our approach may also allow assignment of potential functional classes of neurons. For example,
309 from our examination of voltage-gated potassium channel family gene expression, all are collectively
310 expressed in motor neurons, however the Shab and Shaw genes have more discrete expression
311 patterns in other CNS neuron classes, potentially imbuing these neurons with unique functional
312 characteristics (Chow and Leung, 2020). Future multiplexing of binary genetic expression systems
313 and reporters (Simpson, 2009; del Valle Rodríguez et al., 2011; Diao et al., 2015) should enable
314 neurons or glia to be further quantitively sub-classified by gene expression features throughout the
315 entire intact central nervous system.
316

317 **MATERIALS AND METHODS**

318 **Drosophila stocks**

319 The following stocks were employed - y[1] w[67c23]; Mi{PT-GFSTF.0}Syt1[MI02197-GFSTF.0]/CyO
320 (BDSC#59788)(Venken et al., 2011), y[1] w[*] Mi{y[+mDint2]=MIC}Sh[MI10885] (BDSC#56260), y[1]
321 w[*];Mi{y[+mDint2]=MIC}Shal[MI10881] (BDSC#56089)(Venken et al., 2011), y[1] w[*];
322 Mi{y[+mDint2]=MIC} Shab[MI00848] (BDSC#34115)(Venken et al., 2011), nSyb-
323 GAL4(R57C10)(Pfeiffer et al., 2008), repo-GAL4 (BDSC#7415)(Sepp et al., 2001), repo-QF2
324 (BDSC#66477)(Lin and Potter, 2016), Shaw-TrojanGAL4 (BDSC#60325)(Venken et al., 2011; Li-
325 Kroeger et al., 2018), Ddc-GAL4(BDSC#7009)(Feany and Bender, 2000), TH-
326 GAL4(BDSC#8848)(Friggi-Grelin et al., 2003b), Trh-GAL4(BDSC#38389)(Alekseyenko et al.,
327 2010), UAS_H2A-GFP(Sherer et al., 2020), QUAS_H2B-mCherry(Sherer et al., 2020), Brp-GAL4
328 (this manuscript), UAS_H2A::GFP-T2A-mKok::Caax (this manuscript). All lines were raised on
329 standard media at 25°C, 50%RH.

330 **Generation of Brp-GAL4 exon 2 insertion line.**

331 A GAL4.2 sequence was inserted in genome, immediately after the start codon of the Brp-RD isoform
332 using CRISPR based gene editing employing the following constructs. *Brp gRNA pCDF3:* Two gRNA
333 sequences targeting each side of the insertion location in exon 2 of *brp*, were selected using the
334 FlyCRISPR algorithm (http://flycrispr.molbio.wisc.edu/), consisting of 20 nucleotides each (PAM
335 excluded), and predicted to have minimal off-targets. Each individual 20-nucleotide gRNA sequence

336 were inserted into pCFD3 plasmid (Addgene #49410) using the KLD enzyme mix (New England
337 Biolabs). *Brp-GAL4 insertion construct*: The 7 following PCR amplified fragments were assembled
338 using HIFI technology - (1) 1198bp Homology arm covering 5'UTR until 5' target site; (2) the region
339 between 5' target site and the start codon were amplified from drosophila nos-cas9 (attp2) genomic
340 DNA (a modified Pam sequence was inserted using overlapping primers); (3) Linker-T2A-GAL4.2
341 sequence was amplified from pBID-DSCP-G-GAL4 (Wang et al., 2012) (the linker-T2A sequence
342 was added upstream of the forward primer); (4) P10-3'UTR was amplified from pJFRC81-10XUAS-
343 IVS-Syn21-GFP-p10 (Addgene 36432); (5) 3xP3-Hsp70pro-dsRed2-SV40polyA selection cassette,
344 flanked by two LoxP sites, was amplified from pHD-sfGFP Scareless dsRed (Addgene 80811); (6)
345 The region covering the end of DsRed cassette until 3' target site and (7) the 1079bp Homology arm
346 2 covering from the 3' target site to exon 2, were amplified from Drosophila nos-cas9 (attp2) genomic
347 DNA. Full length assembly was topo cloned in zero-blunt end pCR4 vector (Invitrogen), all constructs
348 have been verified by sequencing (Microsynth AG, Switzerland) and injections were carried out into
349 a nos-cas9 [attp2] strain (Ren et al., 2013). Correct insertion of GAL4 was verified by genome
350 sequencing. All primer sequences are included in the Key Reagents table.

351 **Construction of UAS_H2A::GFP-T2A-mKok::Caax**

352 PCR amplifications were performed using Platinium Superfi polymerase (Invitrogen). The three PCR
353 fragments were assembled together using Hifi technology (Invitrogen) - (1) Histone2A (H2A) cDNA
354 was amplified from *pDESTP10 LexO-H2A-GFP* template [Gift from Steve Stowers] with a synthetic
355 5'UTR sequence (syn21) added upstream to H2A on the forward primer; (2) sfGFP was amplified
356 from template pHD-sfGFP Scareless dsRed (Addgene 80811) and (3) mKok amplified from pCS2+
357 ChMermaid S188 (Addgene 53617) with the CAAX membrane tag sequence (Sutcliffe et al., 2017)
358 added at the 3' end of the protein using the reverse primer. A *Thosea asigna* virus 2A(T2A) self-
359 cleaving peptide sequence (Diao et al., 2015), was inserted between sfGFP and mKok, using sfGFP
360 reverse and mKok forward overlapping primers. The full length assembly was TOPO cloned into
361 pCR8GW-TOPO vector (Invitrogen) generating pCR8GW-H2A::GFP-T2A-mKok::Caax. The insert,
362 H2A::GFP-T2A-mKok::Caax was , then, transferred to pBID_UASC_G destination vector (Wang et
363 al., 2012) using LR II clonase kit (Invitrogen) to generate pBID_UAS-H2A::GFP-T2A-mKok::Caax.

364 The transgene was generated by injection into the JK66B landing site. All primer sequences are
365 included in the Key Reagents table.

366 **Generation of novel Trojan GAL4 lines.**

367 The MiMIC lines generated by the group of Hugo Bellen(Venken et al., 2011) were acquired from
368 the Bloomington Stock Center. Conversion of Mimic lines to Trojan GAL4 lines lines was performed
369 as described previously (Diao et al., 2015).

370 **Larval CNS preparation and image acquisition**

371 Wandering 3rd instar larvae were dissected in 1x PBS (Mediatech) and fixed with 4% formaldehyde
372 (Sigma-Aldrich) for 20 mins. 1x PBS were added to remove the fixative, and then the CNS was
373 dissected(Hafer and Schedl, 2006) and rinsed with 1xPBS with 4% Triton-X 100 for 2 days at 4°C.
374 After rinses, the CNS was embedded in 1% low melting temperature agarose (Peq gold) mixed with
375 200nm red fluorescent beads (1:50000), then introduced into a glass capillary and positioned well
376 separated from each other. After solidification of the agarose, the capillary was mounted to sample
377 holder, transferred to a Zeiss Lightsheet Z.1 microscope and the samples were extruded from the
378 capillary for imaging. CNS images were acquired with a 20x/1.0 Apochromat immersion detection
379 objective and two 10x/0.2 illumination objectives at 5 different views, with 1μm z-intervals. Voxel
380 resolution was 0.317um.

381 **Image processing and data analysis**

382 Collected multiview datasets were registered and fused with the Fiji Multiview Reconstruction
383 plugin(Preibisch et al., 2010; Schindelin et al., 2012). Image datasets after Multi-view deconvolution
384 were analyzed with Vision4D 3.0.0 (Arivis AG). A curvature flow filter was first used to denoise the
385 image dataset. Subsequently, a Blob Finder algorithm(Najman and Couprie, 2003) was applied to
386 detect and segment bright rounded 3D sphere-like structures in the images with 4.5μm set as the
387 diameter. Segmented objects with volume less than 15μm^3 were removed from analysis by
388 segmentation filter to avoid unspecific signals. Subsequently, the number of nuclei and the x, y, z
389 coordinates of the center geometry of each nucleus were output from Vision4D. Where manual
390 counting was employed (Figure 1 and a randomly selected Brp-GAL4 labelled CNS), Vision4D was
391 used to visualize and iteratively proceed through and manually annotate the dataset. Example whole

CNS datasets where functional neurons or glia are labelled are available (Jiao and McCabe, 2021a, 2021b). In 2D representations, Z position is indicated by colour coding using the scheme below.

Mathematical analysis

The topological summaries methods employed have previously been introduced (Edelsbrunner and Harer, 2010; Ghrist, 2014; Rabadan and Blumberg, 2019; Chazal and Michel, 2021). For a motivating example of the principles underlying topological summaries, one could think of pearls forming a necklace. Topological summaries express the global structure of the necklace formed by the relationships between the positions of the individual pearls, but are invariant under translation and rotation of the necklace overall. Two such necklaces have topological summaries that are comparable even if the pearls in one have no relationship to the pearls in the other. It is the global structures – such as its circular shape on a large scale, or bulges on a smaller scale – formed by the relationships of the individual pearls of each one that matter.

We trained a machine learning classifier, specifically an SVM (support vector machine), on the CNS nuclei positions, in order to evaluate its power in determining characteristics of the animal from which it was derived. The data encompassed all point clouds generated from all CNS lines (Brp-Gal4, Syt-Gal4, nSyb-Gal4, Repo-Gal4). Correlation significance (classification power) is determined by comparing the performance of the SVM on the actual classification task to one wherein each larva is randomly assigned a class.

Mathematically speaking, the nuclei positions from a single CNS form a point cloud, a finite set of points in R^3. A possible, naive approach to SVM feature selection for point clouds would be to consider the mean, variance, or other modes of the distribution of pairwise distances within the cloud. These real-valued features could then be passed through, for example, radial basis function kernels for use in SVMs. We focused on very different kind of features, namely ones obtained from the

topology of the point clouds. When the point cloud is of low dimension, such as the three-dimensional point clouds arising from nuclei position data, the following approach is relevant. Let X be a finite point cloud in R^3. For any $r \geq 0$, we let X_r denote the same point cloud, but with each point replaced by a ball of radius r. As r increases, the sequence formed by the X_r expresses different topological features of X. By topological features, we here mean the presence or absence of multiple connected components, unfilled loops, and unfilled cavities.

The figure below illustrates this process in the case of a synthetic 2-dimensional point cloud, but the idea extends to any dimension including whole CNS point clouds. When r is small, X_r is topologically very similar to $X = X_0$, and is essentially a collection of disjoint points. When r is very large, X_r is topologically very similar to X_∞, i.e., one giant, featureless blob. As the sequence X_r progresses through the continuum of scales between these two trivial extremes, it undergoes non- trivial topological changes: components merge, and loops form and later get filled. In higher dimensions, cavities of various dimensions likewise form and get filled in.

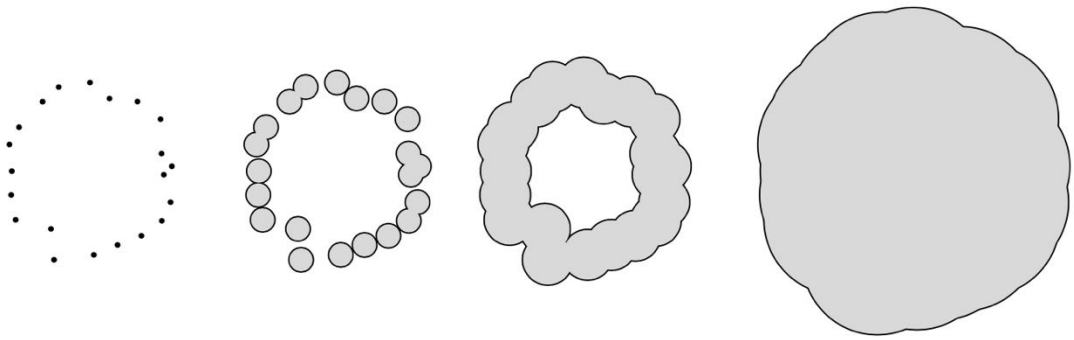

A small 2-dimensional point cloud X viewed at four different scales $0 < a < b < c$, forming the filtration $X = X_0 \subset X_a \subset X_b \subset X_c$.

In the parlance of topological data analysis (TDA), we refer to this appearance and disappearance of topological structures as the *birth* and *death* of homology classes in various degrees. We capture the whole life cycle with a mathematical object called the *persistent homology* of the point cloud, which can be fully described by its *persistence diagram*, a planar collection of points (labelled by

multiplicity), whose coordinates encode the birth and death of homological features. For the filtration in the figure above, the persistence diagram that tracks 1-dimensional features (i.e., unfilled loops) contains only a single point with coordinates (x, y). Here the first coordinate, x, is the radius at which the loop is first formed, and the second coordinate, y, is the radius at which the loop has just been filled in. In the example it is clear that $a < x < b < y < c$.

As multisets of points in the plane, persistence diagrams are not immediately usable as features for SVMs. One way to vectorize persistence diagrams and thus render them digestible by SVMs is to define kernels based on the diagrams, with the heat kernel (Reininghaus et al., 2015) being an oft-used candidate with nice properties. For persistence diagrams P and Q, the heat kernel can informally be defined by the inner product of two solutions of the heat equation — one with an initial condition defined by P, and the other with one defined by Q.

In this analysis in this manuscript, we calculated the persistent homology of the alpha complex (Edelsbrunner and Mücke, 1994) of the point clouds, using GUDHI(The GUDHI Editorial Board, n.d.). The heat kernels were computed using RFPKOG (Spreemann, 2021). Only the persistence diagrams in degree 1 were used. Since the number of whole CNS point clouds was relatively small, we subsampled each one randomly to 8000 points 100 times, producing a total of 3100 point clouds. This was done both in order to test the stability of the method and to ensure that the variability in the number of points in each cloud is not the source of any signal.

The hyperparameters involved, i.e., the SVM regularizer and the heat kernel bandwidth, were determined by a parameter search in the following way. Six point clouds from males and six from females were randomly selected. All 100 subsampled versions of each of these 12 constituted a training set, for a total of 1200 training point clouds. The remaining 1900 subsampled point clouds constituted the testing set. The Pearson correlation between the gender predicted by the SVM on the testing set and the ground truth was computed for each choice of hyperparameters, and a choice in a stable region with high correlation was selected: a regularization parameter $C = 10$ in the notation

466 of Pedregosa *et al* (Pedregosa et al., 2011) and a bandwidth of σ = 1/100 in the notation of
467 Reininghaus *et al* (Reininghaus et al., 2015). For the simple distance distribution features, a similar
468 parameter selection process yielded C=10 and a radial kernel bandwidth of 10^5.

469 **Immunofluorescence Staining and confocal microscopy**

470 Embryos were collected and staged at 25°C on apple agar plates supplemented with yeast paste.
471 Standard methods were used for dechorionation, removal of the vitelline membrane and
472 fixation(Bashaw, 2010). Embryos were stored in 100 % ethanol at -20°C before IHC labelling.
473 Embryos were stained with mouse anti-myc^{9EH10} (1:100, DSHB), visualised with goat anti-
474 mouse::AF488 (1:400, Jackson ImmunoResearch) together with conjugated goat anti-HRP::AF647
475 (1:200, Jackson ImmunoResearch) and mounted in VectorShield (Vector Laboratories). Duel
476 colour Z-stack images of stage 15/16 and late stage 17 embryos were obtained on a CSU-W1
477 Confocal Scanner Unit (Yokogowa, JPN) using two prime BSI express cameras (Teledyne
478 Photometrics). For motor neuron and adult brain preparation, larval fillets from the 3rd instar larvae,
479 or brains from adults were dissected and fixed with 4% formaldehyde (Sigma-Aldrich) for 20 mins.
480 After fixation, samples were rinsed with 1x PBS and were washed in PBT overnight at 4°C, and
481 then mounted in VECTASHIELD antifade mounting medium. Z-stack images were taken from
482 Leica SP8 upright confocal microscope.
483 For Deadpan staining, brains from the 3rd instar larvae were dissected out and fixed with 4% PFA
484 for 20 mins. After fixation, samples were rinsed with 1x PBS, and permealized with PBT (1xPBS +
485 4% Triton-X 100). Antibody stainings were done in PBT + 5% normal goat serum. The dilution for
486 chicken anti-GFP (Abcam) is 1:500, for rat anti-Deadpan (Abcam) is 1: 50. Alexa Fluor 488 anti-
487 chicken, and Alexa Fluor 594 anti-rat secondary antibodies were obtained from ThermoFisher and
488 used at the 1:500 dilutions. Brains were mounted in VECTASHIELD antifade mounting medium,
489 and imaged with Leica SP8.
490

491 **Statistical Analysis**

Column statistics analyses were performed using GraphPad Prism 9 (GraphPad Software). For Figure 1, statistical significance was determined by unpaired t test. For Figure 2,3,4, statistical significances were determined by Ordinary one-way ANOVA, followed by a Tukey's honestly significant difference test when multiple comparisons were required. The distribution analysis in Figure 2 were performed using matlab (MathWorks). Distances between nuclei coordinates were calculated in matlab using code available at https://doi.org/10.5281/zenodo.6574838 and plotted as a histogram of distance distribution.

ACKNOWLEDGEMENTS: This work was supported in part using the resources and services of the BioImaging & Optics Platform (BIOP) Research Core Facility at the School of Life Sciences of EPFL and we are especially thankful for the assistance of Arne Seitz. We are grateful to Hugo Bellen, Benjamin White, Gerry Rubin, Vanessa Auld, Christopher Potter, Mel Feany, Serge Birman, Ed Kravitz, Chris Doe and Pavel Tomancak for generating Drosophila stocks, software and providing advice. Stocks obtained from the Bloomington Drosophila Stock Center (NIH P40OD018537) were used in this study.

AUTHOR CONTRIBUTIONS: W.J, G.S, E.R, S.B, J.A, Y.S., S.S, K.H. and B.M. conceived and designed the study. W.J performed the majority of experiments and analysed the data, assisted by G.S. and Y.S. E.R. generated all novel transgenes, the Brp>GAL4 genome edit and generated illustrations. S.B. generated the Syt1 Trojan line and other useful reagents and SV imaged embryos. S.S. generated the histone fusion transgenes. W.J., G.S, K.H. and B.M. wrote the manuscript

FUNDING: This work was supported by the Swiss National Science Foundation grant number: 31003A_179587 to B.M.

DATA AND MATERIALS AVAILABILITY: All genetic and molecular reagents are described in the Key Resources Table. Drosophila lines not available from public stock centers are freely available upon request – see https://www.epfl.ch/labs/mccabelab/resources/. Individual whole CNS quantitation data is available as source data files associated with each figure. Matlab code is available at https://doi.org/10.5281/zenodo.6574838. Example unprocessed whole CNS microscopy data is publicly available for neurons - doi:10.5281/zenodo.5585334 and for glia doi:10.5281/zenodo.5585358.

REFERENCES

Ainsley JA, Kim MJ, Wegman LJ, Pettus JM, Johnson WA. 2008. Sensory mechanisms controlling the timing of larval developmental and behavioral transitions require the Drosophila DEG/ENaC subunit, Pickpocket1. *Dev Biol* **322**:46–55. doi:10.1016/j.ydbio.2008.07.003

Alekseyenko OV, Lee C, Kravitz EA. 2010. Targeted Manipulation of Serotonergic Neurotransmission Affects the Escalation of Aggression in Adult Male Drosophila melanogaster. *PLOS ONE* **5**:e10806. doi:10.1371/journal.pone.0010806

Aleman-Meza B, Jung S-K, Zhong W. 2015. An automated system for quantitative analysis of Drosophila larval locomotion. *BMC Dev Biol* **15**:11. doi:10.1186/s12861-015-0062-0
Alivisatos AP, Chun M, Church GM, Greenspan RJ, Roukes ML, Yuste R. 2012. The brain activity map project and the challenge of functional connectomics. *Neuron* **74**:970–974. doi:10.1016/j.neuron.2012.06.006

Allen AM, Neville MC, Birtles S, Croset V, Treiber CD, Waddell S, Goodwin SF. 2020. A single-cell transcriptomic atlas of the adult Drosophila ventral nerve cord. *eLife* **9**:e54074. doi:10.7554/eLife.54074

Aso Y, Sitaraman D, Ichinose T, Kaun KR, Vogt K, Belliart-Guérin G, Plaçais P-Y, Robie AA, Yamagata N, Schnaitmann C, Rowell WJ, Johnston RM, Ngo T-TB, Chen N, Korff W, Nitabach MN, Heberlein U, Preat T, Branson KM, Tanimoto H, Rubin GM. 2014. Mushroom body output neurons encode valence and guide memory-based action selection in Drosophila. *eLife* **3**:e04580. doi:10.7554/eLife.04580

Baines RA, Bate M. 1998. Electrophysiological Development of Central Neurons in the *Drosophila* Embryo. *J Neurosci* **18**:4673–4683. doi:10.1523/JNEUROSCI.18-12-04673.1998

Bashaw GJ. 2010. Visualizing Axons in the Drosophila Central Nervous System Using Immunohistochemistry and Immunofluorescence. *Cold Spring Harb Protoc* **2010**:pdb.prot5503.

Bates AS, Janssens J, Jefferis GS, Aerts S. 2019. Neuronal cell types in the fly: single-cell anatomy meets single-cell genomics. *Curr Opin Neurobiol*, Neuronal Identity **56**:125–134. doi:10.1016/j.conb.2018.12.012

Bellen HJ, Tong C, Tsuda H. 2010. 100 years of Drosophila research and its impact on vertebrate neuroscience: a history lesson for the future. *Nat Rev Neurosci* **11**:514–522. doi:10.1038/nrn2839
Berger C, Renner S, Lüer K, Technau GM. 2007. The commonly used marker ELAV is transiently expressed in neuroblasts and glial cells in the Drosophila embryonic CNS. *Dev Dyn Off Publ Am Assoc Anat* **236**:3562–3568. doi:10.1002/dvdy.21372

Bier E, Vaessin H, Younger-Shepherd S, Jan LY, Jan YN. 1992. deadpan, an essential pan-neural gene in Drosophila, encodes a helix-loop-helix protein similar to the hairy gene product. *Genes Dev* **6**:2137–2151. doi:10.1101/gad.6.11.2137

Birkholz O, Rickert C, Nowak J, Coban IC, Technau GM. 2015. Bridging the gap between postembryonic cell lineages and identified embryonic neuroblasts in the ventral nerve cord of Drosophila melanogaster. *Biol Open* **4**:420–434. doi:10.1242/bio.201411072

Brand AH, Perrimon N. 1993. Targeted gene expression as a means of altering cell fates and generating dominant phenotypes. *Development* **118**:401–415.

Chazal F, Michel B. 2021. An Introduction to Topological Data Analysis: Fundamental and Practical Aspects for Data Scientists. *Front Artif Intell* **4**.

Chiang A-S, Lin Chih-Yung, Chuang C-C, Chang H-M, Hsieh C-H, Yeh C-W, Shih C-T, Wu J-J, Wang G-T, Chen Y-C, Wu Cheng-Chi, Chen G-Y, Ching Y-T, Lee P-C, Lin Chih-Yang, Lin H-H, Wu Chia-Chou, Hsu H-W, Huang Y-A, Chen J-Y, Chiang H-J, Lu C-F, Ni R-F, Yeh C-Y, Hwang J-K. 2011. Three-Dimensional Reconstruction of Brain-wide Wiring Networks in Drosophila at Single-Cell Resolution. *Curr Biol* **21**:1–11. doi:10.1016/j.cub.2010.11.056

Chow LWC, Leung Y-M. 2020. The versatile Kv channels in the nervous system: actions beyond action potentials. *Cell Mol Life Sci CMLS* **77**:2473–2482. doi:10.1007/s00018-019-03415-8
Covarrubias M, Wei A, Salkoff L. 1991. Shaker, Shal, Shab, and Shaw express independent K+ current systems. *Neuron* **7**:763–773. doi:10.1016/0896-6273(91)90279-9

Davies LR, Schou MF, Kristensen TN, Loeschcke V. 2018. Linking developmental diet to adult foraging choice in Drosophila melanogaster. *J Exp Biol* **221**. doi:10.1242/jeb.175554
Deitcher DL, Ueda A, Stewart BA, Burgess RW, Kidokoro Y, Schwarz TL. 1998. Distinct requirements for evoked and spontaneous release of neurotransmitter are revealed by mutations in the Drosophila gene neuronal-synaptobrevin. *J Neuroscience* **18**:2028–2039.

del Valle Rodríguez A, Didiano D, Desplan C. 2011. Power tools for gene expression and clonal analysis in Drosophila. *Nat Methods* **9**:47–55. doi:10.1038/nmeth.1800

Deniz ÖG, Altun G, Kaplan AA, Yurt KK, von Bartheld CS, Kaplan S. 2018. A concise review of optical, physical and isotropic fractionator techniques in neuroscience studies, including recent developments. *J Neurosci Methods* **310**:45–53. doi:10.1016/j.jneumeth.2018.07.012

Devor A, Bandettini PA, Boas DA, Bower JM, Buxton RB, Cohen LB, Dale AM, Einevoll GT, Fox PT, Franceschini MA, Friston KJ, Fujimoto JG, Geyer MA, Greenberg JH, Halgren E, Hämäläinen MS, Helmchen F, Hyman BT, Jasanoff A, Jernigan TL, Judd LL, Kim S-G, Kleinfeld D, Kopell NJ, Kutas M, Kwong KK, Larkum ME, Lo EH, Magistretti PJ, Mandeville JB, Masliah E, Mitra PP, Mobley WC, Moskowitz MA, Nimmerjahn A, Reynolds JH, Rosen BR, Salzberg BM, Schaffer CB, Silva GA, So PTC, Spitzer NC, Tootell RB, Van Essen DC, Vanduffel W, Vinogradov SA, Wald LL, Wang LV, Weber B, Yodh AG. 2013. The Challenge of Connecting the Dots in the B.R.A.I.N. *Neuron* **80**:270–274. doi:10.1016/j.neuron.2013.09.008

Diao Fengqiu, Ironfield H, Luan H, Diao Feici, Shropshire WC, Ewer J, Marr E, Potter CJ, Landgraf M, White BH. 2015. Plug-and-Play Genetic Access to Drosophila Cell Types using Exchangeable Exon Cassettes. *Cell Rep* **10**:1410–1421. doi:10.1016/j.celrep.2015.01.059

Doe CQ. 2017. Temporal Patterning in the Drosophila CNS. *Annu Rev Cell Dev Biol* **33**:219–240. doi:10.1146/annurev-cellbio-111315-125210

Edelsbrunner H, Harer J. 2010. Computational Topology: An Introduction. doi:10.1007/978-3-540-33259-6_7

Edelsbrunner H, Mücke EP. 1994. Three-dimensional alpha shapes. *ACM Trans Graph* **13**:43–72. doi:10.1145/174462.156635

Eichler K, Li F, Litwin-Kumar A, Park Y, Andrade I, Schneider-Mizell CM, Saumweber T, Huser A, Eschbach C, Gerber B, Fetter RD, Truman JW, Priebe CE, Abbott LF, Thum AS, Zlatic M, Cardona A. 2017. The complete connectome of a learning and memory centre in an insect brain. *Nature* **548**:175–182. doi:10.1038/nature23455

Eschbach C, Zlatic M. 2020. Useful road maps: studying Drosophila larva's central nervous system with the help of connectomics. *Curr Opin Neurobiol*, Whole-brain interactions between neural circuits **65**:129–137. doi:10.1016/j.conb.2020.09.008

Expert P, Lord L-D, Kringelbach ML, Petri G. 2019. Editorial: Topological Neuroscience. *Netw Neurosci* **3**:653–655. doi:10.1162/netn_e_00096

Feany MB, Bender WW. 2000. A Drosophila model of Parkinson's disease. *Nature* **404**:394–398. doi:10.1038/35006074

Friggi-Grelin F, Coulom H, Meller M, Gomez D, Hirsh J, Birman S. 2003a. Targeted gene expression in Drosophila dopaminergic cells using regulatory sequences from tyrosine hydroxylase. *J Neurobiol* **54**:618–627. doi:10.1002/neu.10185

Friggi-Grelin F, Iché M, Birman S. 2003b. Tissue-specific developmental requirements of Drosophila tyrosine hydroxylase isoforms. *genesis* **35**:175–184. doi:10.1002/gene.10178
Gerber B, Stocker RF, Tanimura T, Thum AS. 2009. Smelling, Tasting, Learning: Drosophila as a Study Case In: Korsching S, Meyerhof W, editors. Chemosensory Systems in Mammals, Fishes, and Insects, Results and Problems in Cell Differentiation. Berlin, Heidelberg: Springer. pp. 187–202. doi:10.1007/400_2008_9

Ghrist R. 2014. Elementary Applied Topology, 1st edition. ed. s. l.
Gowda SBM, Salim S, Mohammad F. 2021. Anatomy and Neural Pathways Modulating Distinct Locomotor Behaviors in Drosophila Larva. *Biology* **10**. doi:10.3390/biology10020090

Hafer N, Schedl P. 2006. Dissection of Larval CNS in Drosophila Melanogaster. *J Vis Exp JoVE* 85. doi:10.3791/85

Jazin E, Cahill L. 2010. Sex differences in molecular neuroscience: from fruit flies to humans. *Nat Rev Neurosci* **11**:9–17. doi:10.1038/nrn2754

Jenett A, Rubin GM, Ngo T-TB, Shepherd D, Murphy C, Dionne H, Pfeiffer BD, Cavallaro A, Hall D, Jeter J, Iyer N, Fetter D, Hausenfluck JH, Peng H, Trautman ET, Svirskas RR, Myers EW, Iwinski ZR, Aso Y, DePasquale GM, Enos A, Hulamm P, Lam SCB, Li H-H, Laverty TR, Long F, Qu L, Murphy SD, Rokicki K, Safford T, Shaw K, Simpson JH, Sowell A, Tae S, Yu Y, Zugates CT. 2012. A GAL4-driver line resource for Drosophila neurobiology. *Cell Rep* **2**:991–1001. doi:10.1016/j.celrep.2012.09.011

Jiao W, McCabe BD. 2021a. Whole Brain Drosophila Larval Neurons. doi:10.5281/zenodo.5585334

Jiao W, McCabe BD. 2021b. Whole Brain Drosophila Larval Glia. doi:10.5281/zenodo.5585358
Kaiser M. 2015. Neuroanatomy: Connectome Connects Fly and Mammalian Brain Networks. *Curr Biol* **25**:R416–R418. doi:10.1016/j.cub.2015.03.039

Keller D, Erö C, Markram H. 2018. Cell Densities in the Mouse Brain: A Systematic Review. *Front Neuroanat* **12**. doi:10.3389/fnana.2018.00083

Kimura K-I, Ote M, Tazawa T, Yamamoto D. 2005. Fruitless specifies sexually dimorphic neural circuitry in the Drosophila brain. *Nature* **438**:229–233. doi:10.1038/nature04229

Kremer MC, Jung C, Batelli S, Rubin GM, Gaul U. 2017. The glia of the adult Drosophila nervous system. *Glia* **65**:606–638. doi:10.1002/glia.23115

Lacin H, Chen H-M, Long X, Singer RH, Lee T, Truman JW. 2019. Neurotransmitter identity is acquired in a lineage-restricted manner in the Drosophila CNS. *eLife* **8**:e43701. doi:10.7554/eLife.43701

Lent R, Azevedo FAC, Andrade-Moraes CH, Pinto AVO. 2012. How many neurons do you have? Some dogmas of quantitative neuroscience under revision. *Eur J Neurosci* **35**:1–9. doi:https://doi.org/10.1111/j.1460-9568.2011.07923.x

Li H, Janssens J, De Waegeneer M, Kolluru SS, Davie K, Gardeux V, Saelens W, David FPA, Brbić M, Spanier K, Leskovec J, McLaughlin CN, Xie Q, Jones RC, Brueckner K, Shim J, Tattikota SG, Schnorrer F, Rust K, Nystul TG, Carvalho-Santos Z, Ribeiro C, Pal S, Mahadevaraju S, Przytycka TM, Allen AM, Goodwin SF, Berry CW, Fuller MT, White-Cooper H, Matunis EL, DiNardo S, Galenza A, O'Brien LE, Dow JAT, FCA Consortium§, Jasper H, Oliver B, Perrimon N, Deplancke B, Quake SR, Luo L, Aerts S, Agarwal D, Ahmed-Braimah Y, Arbeitman M, Ariss MM, Augsburger J, Ayush K, Baker CC, Banisch T, Birker K, Bodmer R, Bolival B, Brantley SE, Brill JA, Brown NC, Buehner NA, Cai XT, Cardoso-Figueiredo R, Casares F, Chang A, Clandinin TR, Crasta S, Desplan C, Detweiler AM, Dhakan DB, Donà E, Engert S, Floc'hlay S, George N, González-Segarra AJ, Groves AK, Gumbin S, Guo Y, Harris DE, Heifetz Y, Holtz SL, Horns F, Hudry B, Hung R-J, Jan YN, Jaszczak JS, Jefferis GSXE, Karkanias J, Karr TL, Katheder NS, Kezos J, Kim AA, Kim SK, Kockel L, Konstantinides N, Kornberg TB, Krause HM, Labott AT, Laturney M, Lehmann R, Leinwand S, Li J, Li JSS, Li Kai, Li Ke, Li L, Li T, Litovchenko M, Liu H-H, Liu Y, Lu T-C, Manning J, Mase A, Matera-Vatnick M, Matias NR, McDonough-Goldstein CE, McGeever A, McLachlan AD, Moreno-Roman P, Neff N, Neville M, Ngo S, Nielsen T, O'Brien CE, Osumi-Sutherland D, Özel MN, Papatheodorou I, Petkovic M, Pilgrim C, Pisco AO, Reisenman C, Sanders EN, dos Santos G, Scott K, Sherlekar A, Shiu P, Sims D, Sit RV, Slaidina M, Smith HE, Sterne G, Su Y-H, Sutton D, Tamayo M, Tan M, Tastekin I, Treiber C, Vacek D, Vogler G, Waddell S, Wang W, Wilson RI, Wolfner MF, Wong Y-CE, Xie A, Xu J, Yamamoto S, Yan J, Yao Z, Yoda K, Zhu R, Zinzen RP. 2022. Fly Cell Atlas: A single-nucleus transcriptomic atlas of the adult fruit fly. *Science* **375**:eabk2432. doi:10.1126/science.abk2432

Li-Kroeger D, Kanca O, Lee P-T, Cowan S, Lee MT, Jaiswal M, Salazar JL, He Y, Zuo Z, Bellen HJ. 2018. An expanded toolkit for gene tagging based on MiMIC and scarless CRISPR tagging in Drosophila. *eLife* **7**:e38709. doi:10.7554/eLife.38709

Lin C-C, Potter CJ. 2016. Editing Transgenic DNA Components by Inducible Gene Replacement in Drosophila melanogaster. *Genetics* **203**:1613–1628. doi:10.1534/genetics.116.191783
Lin DM, Goodman CS. 1994. Ectopic and increased expression of Fasciclin II alters motoneuron growth cone guidance. *Neuron* **13**:507–523. doi:10.1016/0896-6273(94)90022-1

Littleton JT, Stern M, Perin M, Bellen HJ. 1994. Calcium dependence of neurotransmitter release and rate of spontaneous vesicle fusions are altered in Drosophila synaptotagmin mutants. *Proc Natl Acad Sci* **91**:10888–10892. doi:10.1073/pnas.91.23.10888

Louis M. 2020. Mini-brain computations converting dynamic olfactory inputs into orientation behavior. *Curr Opin Neurobiol* **64**:1–9. doi:10.1016/j.conb.2019.11.015

Lundell MJ, Hirsh J. 1994. Temporal and Spatial Development of Serotonin and Dopamine Neurons in the Drosophila CNS. *Dev Biol* **165**:385–396. doi:10.1006/dbio.1994.1261
Mao Z, Davis RL. 2009. Eight different types of dopaminergic neurons innervate the Drosophila mushroom body neuropil: anatomical and physiological heterogeneity. *Front Neural Circuits* **3**. doi:10.3389/neuro.04.005.2009

McCormack TJ. 2003. Comparison of K+-channel genes within the genomes of Anopheles gambiae and Drosophila melanogaster. *Genome Biol* 13.

Meinertzhagen IA. 2018. Of what use is connectomics? A personal perspective on the Drosophila connectome. *J Exp Biol* **221**. doi:10.1242/jeb.164954

Najman L, Couprie M. 2003. Watershed Algorithms and Contrast Preservation In: Nyström I, Sanniti di Baja G, Svensson S, editors. Discrete Geometry for Computer Imagery. Berlin, Heidelberg: Springer Berlin Heidelberg. pp. 62–71. doi:10.1007/978-3-540-39966-7_5
Neckameyer WS, Bhatt P. 2016. Protocols to Study Behavior in Drosophila. *Methods Mol Biol Clifton NJ* **1478**:303–320. doi:10.1007/978-1-4939-6371-3_19

Oliveira-Pinto AV, Santos RM, Coutinho RA, Oliveira LM, Santos GB, Alho ATL, Leite REP, Farfel JM, Suemoto CK, Grinberg LT, Pasqualucci CA, Jacob-Filho W, Lent R. 2014. Sexual dimorphism in the human olfactory bulb: females have more neurons and glial cells than males. *PloS One* **9**:e111733. doi:10.1371/journal.pone.0111733

Pedregosa F, Varoquaux G, Gramfort A, Michel V, Thirion B, Grisel O, Blondel M, Prettenhofer P, Weiss R, Dubourg V, Vanderplas J, Passos A, Cournapeau D. 2011. Scikit-learn: Machine Learning in Python. *J Mach Learn Res* 2825–2830.

Pfeiffer BD, Jenett A, Hammonds AS, Ngo T-TB, Misra S, Murphy C, Scully A, Carlson JW, Wan KH, Laverty TR, Mungall C, Svirskas R, Kadonaga JT, Doe CQ, Eisen MB, Celniker SE, Rubin GM. 2008. Tools for neuroanatomy and neurogenetics in Drosophila. *Proc Natl Acad Sci* **105**:9715–9720. doi:10.1073/pnas.0803697105

Preibisch S, Saalfeld S, Schindelin J, Tomancak P. 2010. Software for bead-based registration of selective plane illumination microscopy data. *Nat Methods* **7**:418–419. doi:10.1038/nmeth0610-418
Quiñones-Frías MC, Littleton JT. 2021. Function of Drosophila Synaptotagmins in membrane trafficking at synapses. *Cell Mol Life Sci CMLS* **78**:4335–4364. doi:10.1007/s00018-021-03788-9
Rabadan R, Blumberg AJ. 2019. Topological Data Analysis for Genomics and Evolution: Topology in Biology. Cambridge: Cambridge University Press. doi:10.1017/9781316671665
Raji JI, Potter CJ. 2021. The number of neurons in Drosophila and mosquito brains. *PloS One* **16**:e0250381. doi:10.1371/journal.pone.0250381

Ravenscroft TA, Janssens J, Lee P-T, Tepe B, Marcogliese PC, Makhzami S, Holmes TC, Aerts S, Bellen HJ. 2020. Drosophila Voltage-Gated Sodium Channels Are Only Expressed in Active Neurons and Are Localized to Distal Axonal Initial Segment-like Domains. *J Neurosci* **40**:7999–8024. doi:10.1523/JNEUROSCI.0142-20.2020

Reininghaus J, Huber S, Bauer U, Kwitt R. 2015. A stable multi-scale kernel for topological machine learning2015 IEEE Conference on Computer Vision and Pattern Recognition (CVPR). Presented at the 2015 IEEE Conference on Computer Vision and Pattern Recognition (CVPR). pp. 4741–4748. doi:10.1109/CVPR.2015.7299106

Ren X, Sun J, Housden BE, Hu Y, Roesel C, Lin S, Liu L-P, Yang Z, Mao D, Sun L, Wu Q, Ji J-Y, Xi J, Mohr SE, Xu J, Perrimon N, Ni J-Q. 2013. Optimized gene editing technology for Drosophila melanogaster using germ line-specific Cas9. *Proc Natl Acad Sci* **110**:19012–19017.

Rodrigues MA, Martins NE, Balancé LF, Broom LN, Dias AJS, Fernandes ASD, Rodrigues F, Sucena É, Mirth CK. 2015. Drosophila melanogaster larvae make nutritional choices that minimize developmental time. *J Insect Physiol* **81**:69–80. doi:10.1016/j.jinsphys.2015.07.002

Ryglewski S, Duch C. 2009. Shaker and Shal Mediate Transient Calcium-Independent Potassium Current in a Drosophila Flight Motoneuron. *J Neurophysiol* **102**:3673–3688. doi:10.1152/jn.00693.2009

Scheffer LK, Meinertzhagen IA. 2019. The Fly Brain Atlas. *Annu Rev Cell Dev Biol* **35**:637–653. doi:10.1146/annurev-cellbio-100818-125444

Schindelin J, Arganda-Carreras I, Frise E, Kaynig V, Longair M, Pietzsch T, Preibisch S, Rueden C, Saalfeld S, Schmid B, Tinevez J-Y, White DJ, Hartenstein V, Eliceiri K, Tomancak P, Cardona A. 2012. Fiji: an open-source platform for biological-image analysis. *Nat Methods* **9**:676–682. doi:10.1038/nmeth.2019

Scott K, Brady R, Cravchik A, Morozov P, Rzhetsky A, Zuker C, Axel R. 2001. A chemosensory gene family encoding candidate gustatory and olfactory receptors in Drosophila. *Cell* **104**:661–673. doi:10.1016/s0092-8674(01)00263-x

Sepp KJ, Schulte J, Auld VJ. 2001. Peripheral Glia Direct Axon Guidance across the CNS/PNS Transition Zone. *Dev Biol* **238**:47–63. doi:10.1006/dbio.2001.0411

Sherer LM, Garrett EC, Morgan HR, Brewer ED, Sirrs LA, Shearin HK, Williams JL, McCabe BD, Stowers RS, Certel SJ. 2020. Octopamine neuron dependent aggression requires dVGLUT from dual-transmitting neurons. *PLOS Genet* **16**:e1008609. doi:10.1371/journal.pgen.1008609
Silbereis JC, Pochareddy S, Zhu Y, Li M, Sestan N. 2016. The Cellular and Molecular Landscapes of the Developing Human Central Nervous System. *Neuron* **89**:248–268. doi:10.1016/j.neuron.2015.12.008

Simpson JH. 2009. Chapter 3 Mapping and Manipulating Neural Circuits in the Fly BrainAdvances in Genetics, Genetic Dissection of Neural Circuits and Behavior. Academic Press. pp. 79–143. doi:10.1016/S0065-2660(09)65003-3

Spreemann G. 2021. RFPKOG. *Really Fast Persistence Kernels GPUs*. https://nonempty.org/software/rfpkog/

Südhof TC, Rothman JE. 2009. Membrane fusion: grappling with SNARE and SM proteins. *Science* **323**:474–477. doi:10.1126/science.1161748

Sutcliffe B, Ng J, Auer TO, Pasche M, Benton R, Jefferis GSXE, Cachero S. 2017. Second-Generation Drosophila Chemical Tags: Sensitivity, Versatility, and Speed. *Genetics* **205**:1399–1408. doi:10.1534/genetics.116.199281

The GUDHI Editorial Board. n.d. GUDHI library. *GUDHI Libr*. https://gudhi.inria.fr/
Venken KJT, Schulze KL, Haelterman NA, Pan H, He Y, Evans-Holm M, Carlson JW, Levis RW, Spradling AC, Hoskins RA, Bellen HJ. 2011. MiMIC: a highly versatile transposon insertion resource for engineering Drosophila melanogaster genes. *Nat Methods* **8**:737–743.
Verkhratsky A, Butt A. 2018. The History of the Decline and Fall of the Glial Numbers Legend. *Neuroglia* **1**:188–192. doi:10.3390/neuroglia1010013

von Bartheld CS, Bahney J, Herculano-Houzel S. 2016. The Search for True Numbers of Neurons and Glial Cells in the Human Brain: A Review of 150 Years of Cell Counting. *J Comp Neurol* **524**:3865–3895. doi:10.1002/cne.24040

Wagh DA, Rasse TM, Asan E, Hofbauer A, Schwenkert I, Dürrbeck H, Buchner S, Dabauvalle M-C, Schmidt M, Qin G, Wichmann C, Kittel R, Sigrist SJ, Buchner E. 2006. Bruchpilot, a Protein with Homology to ELKS/CAST, Is Required for Structural Integrity and Function of Synaptic Active Zones in Drosophila. *Neuron* **49**:833–844. doi:10.1016/j.neuron.2006.02.008

Wang J-W, Beck ES, McCabe BD. 2012. A Modular Toolset for Recombination Transgenesis and Neurogenetic Analysis of Drosophila. *PLOS ONE* **7**:e42102. doi:10.1371/journal.pone.0042102

White JG, Southgate E, Thomson JN, Brenner S. 1986. The structure of the nervous system of the nematode Caenorhabditis elegans. *Philos Trans R Soc Lond B Biol Sci* **314**:1–340. doi:10.1098/rstb.1986.0056

Xiong WC, Okano H, Patel NH, Blendy JA, Montell C. 1994. repo encodes a glial-specific homeo domain protein required in the Drosophila nervous system. *Genes Dev* **8**:981–994. doi:10.1101/gad.8.8.981

Key Resources Table				
Reagent type (species) or resource	**Designation**	**Source or reference**	**Identifiers**	**Additional information**
strain, strain background (Escherichia Coli)	One shot top10	Invitrogen	Cat#: C404010	
genetic reagent (*D. melanogaster*)	y[1] w[67c23]; Mi{PT-GFSTF.0}Syt1[MI02197-GFSTF.0]/CyO	Bloomington Drosophila Stock Center PMID: 21985007	BDSC:59788 FLYB: FBal0314405 RRID:BDSC_59788	FlyBase symbol: Mi{PT-GFSTF.0}Syt1$^{MI02197-GFSTF.0}$
genetic reagent (*D. melanogaster*)	y[1] w[*] Mi{y[+mDint2]=MIC}Sh[MI10885]	Bloomington Drosophila Stock Center PMID: 21985007	BDSC:56260 FLYB: FBal0297530 RRID:BDSC_56260	FlyBase symbol: Mi{MIC}Sh^{MI10885}
genetic reagent (*D. melanogaster*)	y[1] w[*];Mi{y[+mDint2]=MIC}Shal[MI10881]	Bloomington Drosophila Stock Center PMID: 21985007	BDSC:56089 FLYB: FBal0295200 RRID:BDSC_56089	FlyBase symbol: Mi{MIC}Shal^{MI10881}
genetic reagent (*D. melanogaster*)	y[1] w[*]; Mi{y[+mDint2]=MIC}Shab[MI00848]	Bloomington Drosophila Stock Center PMID: 21985007	BDSC:34115 FLYB: FBal0249123 RRID:BDSC_34115	FlyBase symbol: Mi{MIC}Shab^{MI00848}
genetic reagent (*D. melanogaster*)	nSyb-GAL4(R57C10)	Bloomington Drosophila Stock Center PMID: 18621688	BDSC: 39171 FBgn0013342 RRID:BDSC_39171	Flybase symbol: P{GMR57C10-GAL4}
genetic reagent (*D. melanogaster*)	repo-GAL4	Bloomington Drosophila Stock Center PMID: 7926782	BDSC:7415 FLYB: FBal0127275 RRID:BDSC_7415	FlyBase symbol: P{GAL4}repo
genetic reagent (*D. melanogaster*)	repo-QF2	Bloomington Drosophila Stock Center doi:10.1534/genetics.116.191783	BDSC:66477 FLYB: FBal0322908 RRID:BDSC_66477	FlyBase symbol: P{ET-QF2.GU}repo

genetic reagent (*D. melanogaster*)	Shaw-GAL4	Bloomington Drosophila Stock Center PMID: 21985007	BDSC:60325 FLYB: FBal0304243 RRID:BDSC_60325	FlyBase symbol: GAL4$^{Shaw-MI01735-TG4.1}$
genetic reagent (*D. melanogaster*)	Ddc-GAL4	Bloomington Drosophila Stock Center doi:10.1006/dbio.1994.1261	BDSC:7009 FLYB: FBtp0012451 RRID:BDSC_7009	FlyBase symbol: P{Ddc-GAL4.L}
genetic reagent (*D. melanogaster*)	TH-GAL4	Bloomington Drosophila Stock Center PMID: 12555273	BDSC:8848 FLYB: FBtp0114847 RRID:BDSC_8848	FlyBase symbol: P{ple-GAL4.F}3
genetic reagent (*D. melanogaster*)	Trh-GAL4	Bloomington Drosophila Stock Center doi:10.1371/journal.pone.0010806	BDSC:38389 FLYB: FBtp0055412 RRID:BDSC_38389	FlyBase symbol: P{Trh-GAL4.long}
genetic reagent (*D. melanogaster*)	UAS>H2A-GFP	Steve Stowers (Montana SU) doi:10.1371/journal.pgen.1008609	FLYB: FBgn0001196	
genetic reagent (*D. melanogaster*)	QUAS>H2A-mCherry	Steve Stowers (Montana SU) doi:10.1371/journal.pgen.1008609	FLYB: FBgn0001196	
genetic reagent (*D. melanogaster*)	Brp-GAL4	This paper, available upon request, https://www.epfl.ch/labs/mccabelab/resources/	FLYB: FBgn0259246	See Materials and Methods, Section 2
genetic reagent (*D. melanogaster*)	Syt1-Gal4	This paper, available upon request, https://www.epfl.ch/labs/mc	FLYB: FBal0314405	See Materials and Methods, Section 4

		cabelab/resources/		
genetic reagent (*D. melanogaster*)	Sh-Gal4	This paper, available upon request, https://www.epfl.ch/labs/mccabelab/resources/	FLYB: FBal0297530	See Materials and Methods, Section 4
genetic reagent (*D. melanogaster*)	Shal-Gal4	This paper, available upon request, https://www.epfl.ch/labs/mccabelab/resources/	FLYB: FBal0249123	See Materials and Methods, Section 4
genetic reagent (*D. melanogaster*)	Shab-Gal4	This paper, available upon request, https://www.epfl.ch/labs/mccabelab/resources/	FLYB: FBal0249123	See Materials and Methods, Section 4
genetic reagent (*D. melanogaster*)	UAS>H2A::GFP-T2A-mKok::Caax	This paper, available upon request, https://www.epfl.ch/labs/mccabelab/resources/	FLYB: FBgn0001196	See Materials and Methods, Section 3
antibody	anti-myc^{9EH10}(Mouse monoclonal)	DSHB	DSHB Cat# 9E10, RRID:AB_2266850	IF(1:100)
antibody	anti-GFP(Chicken polyclonal)	Abcam	Cat#ab13970	IF(1:500)
antibody	anti-Deadpan(Rat monoclonal)	Abcam	Cat#ab195173	IF(1:50)

antibody	Goat Anti-Mouse IgG (H+L), Alexa Fluor 488 (Goat polyclonal Secondary Antibody)	Jackson ImmunoResearch	Cat#115-545-166	IF(1:400)
antibody	Goat Anti-Horseradish Peroxidase, Alexa Fluor 647 (Goat polyclonal)	Jackson ImmunoResearch	Cat#123-605-021	IF(1:200)
antibody	Goat anti-Chicken IgY (H+L), Alexa Fluor 488 (Goat polyclonal Secondary Antibody)	ThermoFisher	Cat#A-11039	IF(1:500)
antibody	Goat anti-Rat IgG (H+L) Cross-Adsorbed, Alexa Fluor 594 (Goat polyclonal Secondary Antibody)	ThermoFisher	Cat#A-11007	IF(1:500)
recombinant DNA reagent	pBID-DSCP-G-Gal4 (plasmid)	McCabe Lab, Available upon request. https://www.epfl.ch/labs/mccabelab/resources/	Cat# #35200	
recombinant DNA reagent	pJFRC81-10XUAS-IVS-Syn21-GFP-p10 (plasmid)	Addgene	Cat#: 36432	
recombinant DNA reagent	pHD-sfGFP Scareless dsRed (plasmid)	Addgene	Cat#: 80811	
recombinant DNA reagent	pCFD3 (plasmid)	Addgene	Cat#: 49410	
recombinant DNA reagent	pCR4 Brp-Gal4	This paper, available upon request, https://www.epfl.ch/labs/mccabelab/resources/		CRISPR construct inserted in D. Melanogaster

recombinant DNA reagent	pBID LexO>H2A-mCherry	Gift from Steve Stowers (Montana SU), DOI: 10.1371/journal.pgen.1008609		
recombinant DNA reagent	pCS2+ ChMermaid S188	Addgene	Cat#: 53617	
recombinant DNA reagent	pBID-UAS>H2A::GFP-T2A-mKok::Caax	This paper, available upon request, https://www.epfl.ch/labs/mccabelab/resources/		construct inserted in D. Melanogaster
sequence-based reagent	pCFD3 gRNA Brp-5'	This paper	Guide RNA for Brp CRISPR knock in	GGTGAACCGACCGG GACAAC
sequence-based reagent	pCFD3 gRNA Brp-3'	This paper	Guide RNA for Brp CRISPR knock in	GGGAGCCCCGCGAC CGCTCC
sequence-based reagent	Brp Ha1 Fo	This paper	PCR primer	GAGAGAGCATCTC GATTGTGCCGTGTG
sequence-based reagent	Brp Pam7 Re	This paper	PCR primer	AATGTTGTCCCGG TCGGTTCACCG
sequence-based reagent	Brp Pam7_In1 Re	This paper	PCR primer	TTCTAGCGTCCAACGG CTCAGCTGTGGGCCAT TTTCTAGTAATGTTGTC CCGGTCGGTTCACCG
sequence-based reagent	Brp HA_In1 Fo	This paper	PCR primer	ACTAGAAAATGGC CCACAGCTGAGCC

sequence-based reagent	Brp V5_In1 Re	This paper	PCR primer	TAGAATCGAG ACCGA GGAGAGGGTT AGGG ATAGGCTTAC CCATT GCTGAAATTC ACA CACACACAGA ATT CATGAG
sequence-based reagent	Brp V5_ Fo	This paper	PCR primer	GGTAAGCCTA TCCCT AACCCTCTCC TC
sequence-based reagent	Brp PB5' Re	This paper	PCR primer	TTAAGGGATC TTTCT ATTAGTATAAC ACTG CATGC
sequence-based reagent	Brp Ex2 fo	This paper	PCR primer	AAATTGCATG CAGTGT TATACTAATAG AAAG ATCCCTTAATC GGCAG TCCATACTACC GCGACATGGA TG
sequence-based reagent	Brp Pam2_Re	This paper	PCR primer	TCTGGAGCGG TCGCGGGGC
sequence-based reagent	Brp Pam2_Brp Ha2 Re	This paper	PCR primer	GCTCGTCCTC TAG GTACAGGCCC CGT TCGAGGGATC TGTC TCTGGAGCGG T CGCGGGG
sequence-based reagent	Brp Ha2 Fo	This paper	PCR primer	GACAGATCCC TCGA ACGGGGCC
sequence-based reagent	Syn21 H2A Fo	This paper	PCR primer	AACTTAAAAAA AAAA

				ATCAAAATGTC TGGA CGTGGAAAAG GTG GC
sequence-based reagent	H2A Re	This paper	PCR primer	CCCAAGAAGA CCGA GAAGAAGGCC
sequence-based reagent	H2A-GFP Fo	This paper	PCR primer	ACAGGCTGTT CTGTT GCCCAAGAAG ACCG AGAAGAAGGC CATG GTGTCCAAGG GCGA GGAG
sequence-based reagent	GFP-T2A Re	This paper	PCR primer	GGGTTCTCCT CCACAT CGCCGCAGGT CAGCA GGCTGCCGCG GCC CTCCTTGTACA GCTCA TCCATGCCCA GG
sequence-based reagent	T2A-mKok Fo	This paper	PCR primer	GCGGCAGCCT GCTGAC CTGCGGCGAT GTGGA GGAGAACCCC GGGCCC ATGGTGAGTG TGATTAA ACCAGAGATG AAGATG
sequence-based reagent	mKok-Caax Re	This paper	PCR primer	TTACATAATTA CACACTT TGTCTTTGACT TCTTTTT CTTCTTTTTAC CATCTTT GCTCATGGAA TGAGCTA CTGCATCTTCT ACCTGC

chemical compound, drug	Formaldehyde 37%	Sigma	Cat#: 252549	
chemical compound, drug	Low melt agarose	Peq gold	Cat#: 35-2010	
chemical compound, drug	VECTASHIELD Antifade Mounting Media	VECTOR Laboratories	Cat#: H-1000	
chemical compound, drug	FluoSpheres, 0.2 µm, red fluorescent (580/605)	Thermo Fisher Scientific	Cat#: F8810	
commercial assay or kit	Zero Blunt™ TOPO™ PCR Cloning Kit	Invitrogen	Cat#: 450245	
commercial assay or kit	pCR™8/GW/TOPO™ TA Cloning Kit	Invitrogen	Cat#: K250020	
commercial assay or kit	Gateway™ LR Clonase™ II Enzyme mix	Invitrogen	Cat#:11791020	
commercial assay or kit	NEBuilder® HiFi DNA Assembly Master Mix	New England Biolabs	Cat#: E2621S	
commercial assay or kit	KLD enzyme mix	New England Biolabs	Cat#:M0554S	
commercial assay or kit	Platinium Superfi polymerase	Invitrogen	Cat#:12359010	
software, algorithm	CNS nuclei distance (code for Matlab)	https://doi.org/10.5281/zenodo		This manuscript
software, algorithm	Fiji	https://fiji.sc/	RRID:SCR_002285	
software, algorithm	Arivis Vision4D 3.0.0	Arivis	RRID:SCR_018000	

software, algorithm	MATLAB R2018a	MathWorks	RRID:SCR_001622	
software, algorithm	GraphPad Prism 9.0	GraphPad	RRID:SCR_002798	